

An Overview of Dual-Phase Steels: Advances in Microstructure-Oriented Processing and Micromechanically Guided Design

C.C. Tasan,¹ M. Diehl,¹ D. Yan,¹ M. Bechtold,²
F. Roters,¹ L. Schemmann,³ C. Zheng,⁴ N. Peranio,⁵
D. Ponge,¹ M. Koyama,⁶ K. Tsuzaki,⁶ and D. Raabe¹

¹Max-Planck-Institut für Eisenforschung GmbH, 40237 Düsseldorf, Germany;
email: raabe@mpie.de

²Salzgitter Mannesmann Forschung GmbH, 38239 Salzgitter, Germany

³Salzgitter Mannesmann Forschung GmbH, 47259 Duisburg, Germany

⁴Institute of Metal Research, Chinese Academy of Sciences, Shenyang 110016, China

⁵Institut für Angewandte Physik, Eberhard Karls Universität Tübingen, 72076 Tübingen, Germany

⁶Department of Mechanical Engineering, Kyushu University, Nishi-ku, Fukuoka 819-0395, Japan

Annu. Rev. Mater. Res. 2015. 45:391–431

First published online as a Review in Advance on April 23, 2015

The *Annual Review of Materials Research* is online at matsci.annualreviews.org

This article's doi:
10.1146/annurev-matsci-070214-021103

Copyright © 2015 by Annual Reviews.
All rights reserved

Keywords

martensite-ferrite, high-strength steel, simulation, micromechanics, multiphase alloys

Abstract

Dual-phase (DP) steel is the flagship of advanced high-strength steels, which were the first among various candidate alloy systems to find application in weight-reduced automotive components. On the one hand, this is a metallurgical success story: Lean alloying and simple thermomechanical treatment enable use of less material to accomplish more performance while complying with demanding environmental and economic constraints. On the other hand, the enormous literature on DP steels demonstrates the immense complexity of microstructure physics in multiphase alloys: Roughly 50 years after the first reports on ferrite-martensite steels, there are still various open scientific questions. Fortunately, the last decades witnessed enormous advances in the development of enabling experimental and simulation techniques, significantly improving the understanding of DP steels. This review provides a detailed account of these improvements, focusing specifically on (*a*) microstructure evolution during processing, (*b*) experimental characterization of micromechanical behavior, and (*c*) the simulation of mechanical behavior, to highlight the critical unresolved issues and to guide future research efforts.

1. INTRODUCTION

Steels are humankind's most important structural materials, enabling technology breakthroughs in various fields, such as energy, transportation, safety, and infrastructure. Profound progress in these fields has been achieved through the development of advanced high-strength steels (AHSS), fueled by the conflicting demands on the automotive industry to simultaneously improve crash safety and fuel economy. The engineering and scientific interest in dual-phase (DP) steel, one of the earliest and most prominent examples of AHSS, has been especially strong in the last decade.

From an engineering perspective, the ongoing interest in DP steel is well justified. With relatively straightforward thermomechanical processing and lean alloying, a notionally simple ferrite-martensite microstructure develops in these steels, which in turn provides a wide range of excellent and industrially accessible mechanical properties. DP steels typically have high ultimate tensile strength (UTS) (enabled by the martensite) combined with low initial yielding stress (enabled by the ferrite), high early-stage strain hardening, and macroscopically homogeneous plastic flow (enabled through the absence of Lüders effects). These features render DP steels ideal alloy systems for automotive-related sheet-forming operations. From a scientific perspective, the research and publication trends suggest that the full potential of DP steels has not been reached. There are still various open questions, especially regarding the through-process microstructure development and the microstructure-property relationships. From this perspective, the term DP belies the complexity of the microstructure of these steels. In fact, their constitution may also incorporate retained austenite, pearlite, bainite, carbides, and acicular ferrite, depending on the processing route. Further complexity is introduced due to various processing- and composition-dependent microstructural parameters, for example, martensite volume fraction (V_M), martensite grain size (S_M), martensite carbon content (C_M), martensite/ferrite morphology, ferrite grain size (S_F), ferrite texture, density of transformation-induced geometrically necessary dislocations (GNDs), micro- and mesoscale segregation, and the chemical decoration state of the heterointerfaces (1–5). This large parameter space determines the mechanical behavior of DP steels, although identifying the exact role of the individual mechanisms is a complex task. Only recently have in-depth data become available through the development of novel experimental microscopic and micromechanical techniques [e.g., electron channeling contrast imaging (ECCI) (**Figure 1b**), electron backscatter diffraction (EBSD) (**Figure 1a**), atom probe tomography (APT) (**Figure 1c**), miniaturized testing, and in situ probing of microstructure evolution; see sidebar: Advances in Microstructure Characterization of Dual-Phase Steels in Section 2 below] and computational approaches [e.g., multiphase crystal plasticity (CP) simulation and kinetic and thermodynamic models based on improved thermodynamic data considering diffusion, phase transformation, and recrystallization]. These advances call for a comprehensive analysis of the state-of-the-art understanding of and the current challenges regarding the microstructure development and properties of DP steels.

This overview of the current understanding of the relationships between processing, microstructure, micromechanics, and mechanical behavior of DP steels aims at guiding industrial and scientific research to concentrate on some of the pending key challenges in this field. The overview is structured in three parts: Section 2 focuses on microstructure evolution of DP steel during processing, Section 3 focuses on experimental observations of the micromechanical behavior of DP steel, and Section 4 focuses on computational description of DP steel mechanical behavior.

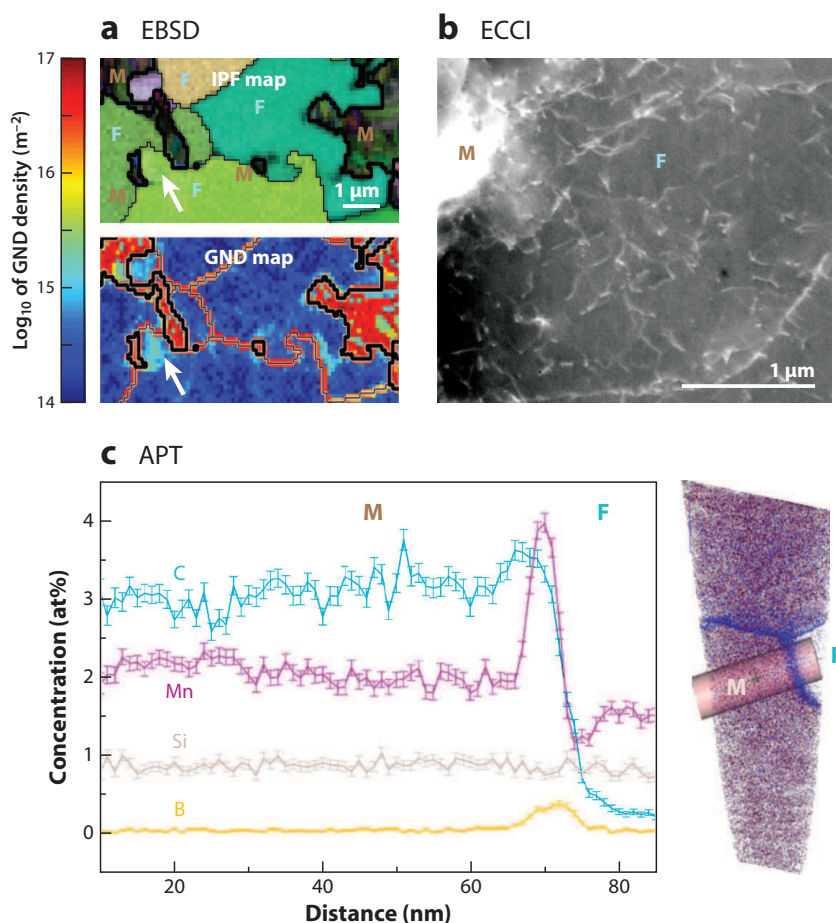


Figure 1

Examples of applications of novel microstructure characterization techniques to DP steels. (a) EBSD-based IPF map and its corresponding calculated GND density. White arrows point to a ferritic region of high GND density due to the transformation of the surrounding martensite islands. (b) ECCI-based dislocation structure imaging through SEM, showing dislocations in a ferrite grain. (c) APT compositional profiles (left) and the reconstructed 3D view of the atomic composition distributions (right) showing heterophase interface segregation of Mn and B. Abbreviations: GND, geometrically necessary dislocation; F, ferrite; IPF, inverse pole figure; M, martensite.

2. MICROSTRUCTURE AND TEXTURE EVOLUTION DURING PROCESSING OF DUAL-PHASE STEELS

2.1. Introduction

To obtain a homogeneous DP steel microstructure with well-dispersed martensite islands and fine primary recrystallized ferrite, a continuous annealing process is typically applied. This process includes reheating of the initial cold-rolled ferrite-pearlite or ferrite-bainite microstructure into the range of intercritical annealing (IA) or rapid austenitic annealing, followed by quenching below the martensite start temperature (Figure 2).

For achieving the desired microstructures, DP steels typically contain 0.06–0.15-wt% C and 1.5–3% Mn (the former strengthens the martensite, the latter causes solid-solution strengthening in ferrite, and both stabilize the austenite), Cr and Mo (to retard pearlite or bainite formation),

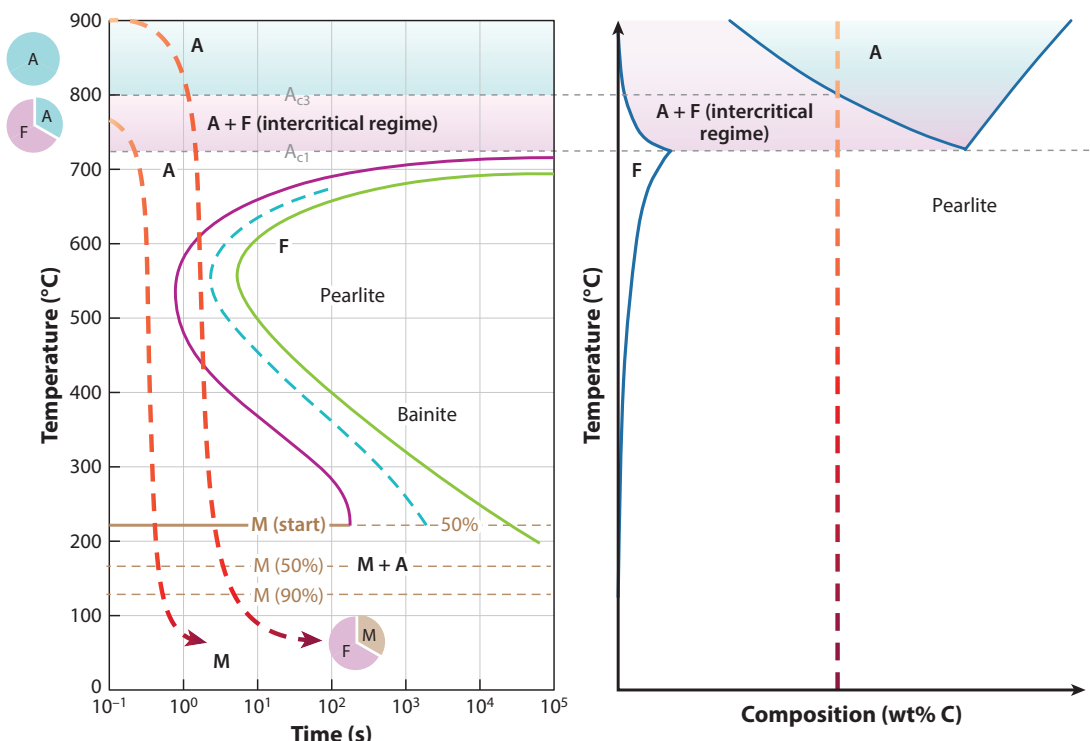


Figure 2

Schematic indicating the heat treatment methods used to obtain a DP ferrite-martensite microstructure. Typically, the final annealing procedure for DP steels consists of holding the material in an austenite-ferrite (intercritical) regime followed by quenching plus holding at temperatures slightly below the martensite start temperature, whereby the austenite fraction transforms into martensite. Another method involves adjusting the quenching rate from the fully austenitic regime so that most of the undercooled austenite transforms to ferrite while the rest becomes martensite. Abbreviations: A, austenite; F, ferrite; M, martensite. The relevant temperatures at which austenite formation starts and ends (A_{c1} , the temperature at which austenite begins to form during heating, and A_{c3} , the temperature at which the transformation of ferrite to austenite is completed during heating) are alloy dependent.

Si (to promote ferrite transformation), and V and Nb (for precipitation strengthening and microstructure refinement). In this section, we review the microstructure and crystallographic texture evolution of DP steels during the critical processing steps, i.e., hot rolling, cold rolling, and heat treatment. Most of the recent studies on DP microstructure with respect to average crystallographic texture evolution (21–25), morphology, and deformation substructure of the constituent ferrite and martensite phases strongly benefit from the recent developments in the characterization methods (see the sidebar entitled Advances in Microstructure Characterization of Dual-Phase Steels, the Appendix, and References 26–29).

Upon hot and cold rolling of steels, substantial through-thickness microstructure and texture inhomogeneity can occur owing to the imposed through-thickness gradients in shear, total deformation, and temperature (30, 31). This inhomogeneity can be partially inherited through the ensuing processing steps (32–34). Microstructure inhomogeneity is often characterized by a continuous change in the initial ferrite-pearlite or partially bainitic microstructures from a banded morphology (1, 35–39) in the sheet center to a heterogeneous distribution near the surface. Therefore, the mechanical properties of the sheets before and after annealing can be anisotropic and dependent on the through-thickness position. We thus review the evolution of the

ADVANCES IN MICROSTRUCTURE CHARACTERIZATION OF DUAL-PHASE STEELS

Advances in various experimental tools and techniques are paving the way toward improved understanding of (*i*) crystallographic structure and defects and (*ii*) local chemistry in DP steels.

With regard to the former, ECCI combines large field of view and high-resolution defect imaging, for example, to image martensitic transformation-induced interface GNDs in ferrite (6, 7). EBSD has become a standard microstructure mapping technique, and multiple approaches are emerging to analyze the vast quantity of data it produces so as to identify key microstructure correlations. For example, DP steel analysis benefits from standard phase identification, GND density measurements (8, 9), and 3D characterization of microstructure morphology (8). The resolution of full-field crystallographic maps can be pushed down to the nanoregime by employing nanobeam diffraction (10, 11), which is especially critical for the analysis of sub-EBSD-resolution features (12, 13), such as interlath austenite films.

With regard to the latter, the local compositional analysis, energy-dispersive X-ray spectroscopy (EDX), when carried out under optimized conditions with plasma cleaning (14), successfully reveals compositional heterogeneities of even interstitial elements. Wavelength-dispersive X-ray spectroscopy (WDS) provides higher sensitivity for light elements [e.g., the spatial resolution for C has been demonstrated down to ~350 nm (15)]. Combined with EBSD, WDS allows for the classification of bainite, martensite, and ferrite (figures 4–18 in Reference 15). WDS also enables the mapping of substitutional elements to unravel prior phase transformations (9). The most remarkable advances in compositional mapping have been achieved by APT, which enables not only atomic-resolution chemical and phase mapping, but also 3D visualization capabilities, which are critical for identifying carbon segregation sites within martensite islands and at interfaces (16–18). Insights from APT are further strengthened upon direct correlation with crystallographic mapping in transmission electron microscopy (TEM) (19, 20).

near-plane-strain-dominated texture evolution of the ferrite phase in the center of hot- and cold-rolled sheets and the shear textures that occur near the surfaces of hot-rolled sheets (40). Hot- and cold-rolled materials with banded ferritic-pearlitic structure typically have a pearlite volume fraction of 15–35%. The plane-strain ferrite texture evolving in the sheet center is characterized both by a strong α -fiber texture (with the {110} direction parallel to the rolling direction) and by a weak γ -fiber texture (with the {111} plane parallel to the sheet plane).

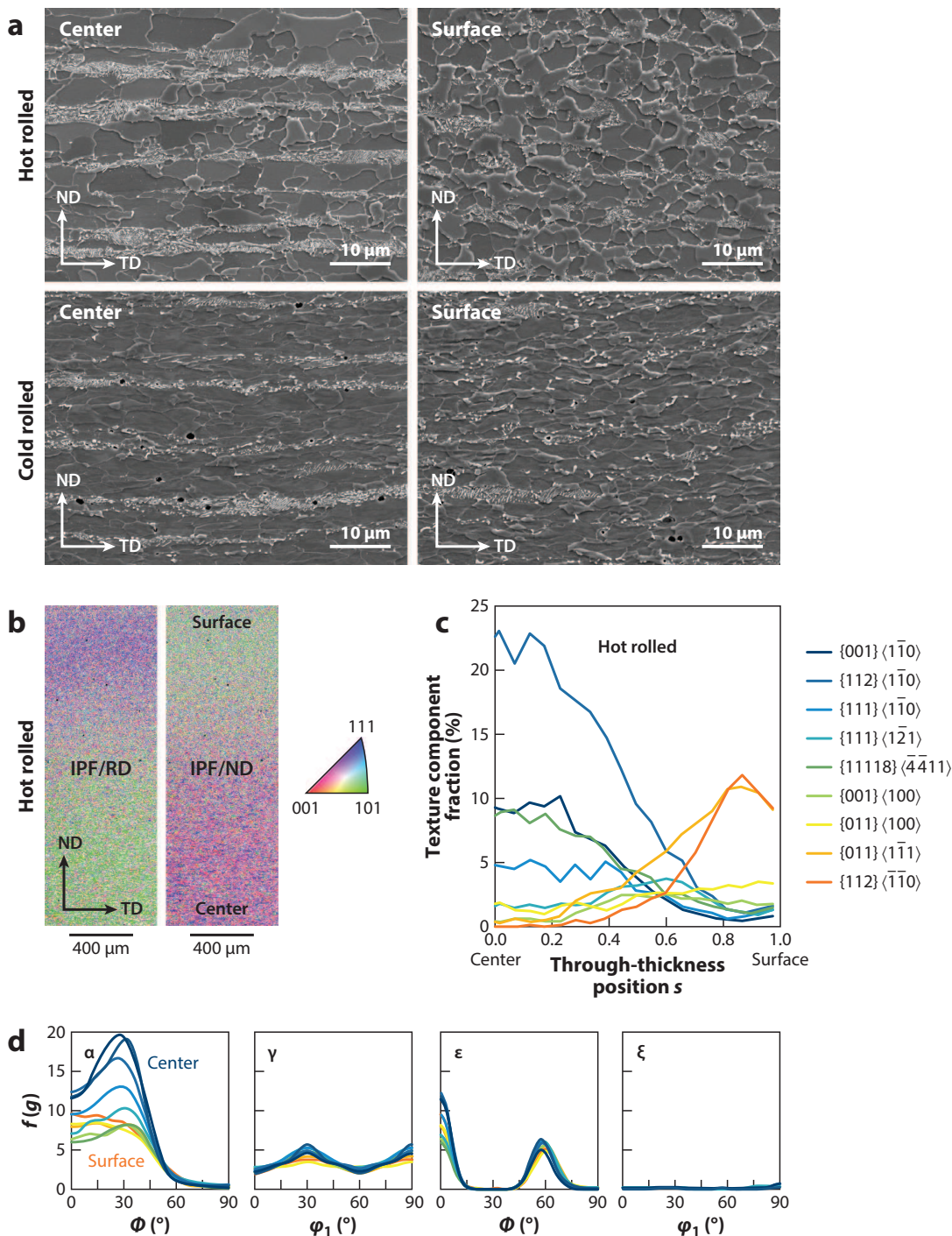
During the final IA, the governing metallurgical mechanisms in DP steels are recovery, recrystallization, diffusion, and phase transformation. The degree of interaction and competition among these phenomena is influenced by (and, hence, can be tailored by adjusting) the heating rate, the annealing temperature and time, and the cooling rate (40–53). For studying these mechanisms and their detailed interactions, various heat treatments have been applied in previous works; such techniques include continuous furnace, salt bath, and conductive annealing for intercritical (as well as austenitic) heating temperatures. For differentiating between the contributions of recovery, recrystallization, diffusion, and phase transformation, spatially resolved experiments (typically based on EBSD mapping) and analytical and full-field mesoscopic simulations have been used (45–55).

2.2. Microstructure and Crystallographic Texture Evolution During Rolling

Figure 3a shows a typical example of microstructure and texture evolution during hot rolling and 75% cold rolling for the sheet center and the near-surface regions of an alloy with 0.147-wt% C, 0.403-wt% Si, and 1.868-wt% Mn. The material had a pearlitic initial hot-band microstructure (40, 41, 56). In the sheet center, proeutectoid ferrite ($S_F \sim 5 \mu\text{m}$) and pearlite ($V_P \sim 40 \text{ vol}\%$) are

distributed in bands along the rolling direction, whereas at the surface the band structure is replaced with a homogeneous mixture of ferrite and pearlite. Chemical probing in a number of rolled sheets revealed that the pearlite bands typically have slightly higher Si and Mn than do the ferrite bands.

Panels *b–d* of Figure 3 give examples of the pronounced texture inhomogeneity, as determined by EBSD, in a transverse section of a hot band. The texture maps are shown as a function of through-thickness position, s , in terms of inverse pole figure (IPF) maps (Figure 3*b*), where each



measurement point is colored according to its IPF value. The texture components are plotted between the sheet center ($s = 0$) and the hot-band sheet surface ($s = 1$) in **Figure 3c**.

For a more quantitative analysis, the orientation distribution function (ODF) can be determined for an Euler angle range $\varphi_1, \phi, \varphi_2 \leq 90^\circ$ (30–34). Hot-band through-thickness texture inhomogeneity is observed for most steel grades (30–34). The Appendix lists important observed texture components. Typically, owing to the gradient in the shear distribution imposed during hot rolling, a plane-strain texture develops in the center ($s = 0$) and a strong shear texture develops close to the surface ($s > 0.7\text{--}0.9$) of the hot bands (30–33, 57) (**Figure 3b–d**). As stated above, the former typically exhibits a strong texture component $\{112\}\langle\bar{1}\bar{1}0\rangle$ (on the α -fiber) and a weaker γ -fiber (**Figure 3c**). The latter, the surface, is characterized by a ζ -fiber with a $\{011\}\langle\bar{1}\bar{1}1\rangle$ component and an ε -fiber with a $\{112\}\langle\bar{1}\bar{1}1\rangle$ component as dominant features, with maximum orientation densities close to the sheet surface ($s \geq 0.9$) (**Figure 3c**). The through-thickness texture inhomogeneity is similar to that observed for corrosion-resistant ferritic stainless steels and Fe-Si soft magnetic transformer steels (30–33).

During cold rolling, the ferrite and pearlite band widths in the center of the sheets decrease with thickness reduction. The ferrite grains become flattened in the normal direction and elongated in the rolling direction. The near-surface ferrite grains undergo the same shape change. Mn-rich cementite precipitates of 200–300 nm are typically observed within the ferrite bands (40) (**Figure 3a**).

Cold rolling typically has two effects on the inherited hot-band textures in DP steels. The first is an improvement in through-thickness texture homogeneity [i.e., an increase in the texture components $\{001\}\langle\bar{1}\bar{1}0\rangle$ and $\{112\}\langle\bar{1}\bar{1}0\rangle$ on the α -fiber, $\{111\}\langle\bar{1}\bar{2}1\rangle$ on the γ -fiber, and $\{11\bar{1}1\}\langle\bar{4}11\rangle$ on the ε -fiber (**Figure 3d**)] such that the pronounced near-surface shear textures are gradually transformed and are rendered more similar to the plane-strain textures observed in the sheet center. The second effect is a strong increase in the orientation gradients within the proeutectoid ferrite grains, as revealed by kernel average misorientation (KAM) maps from the center regions of rolled sheets, which show a larger KAM value within the pancake-shaped proeutectoid ferrite grains than do the center regions of hot-rolled sheets. **Figure 4** shows corresponding microstructure maps of the image quality, IPF, and KAM, all obtained by EBSD in the center region of both hot- and cold-rolled sheets.

2.3. Microstructure and Texture Evolution During Intercritical and Austenitic Annealing

The final annealing procedure for DP steels, the creation of a ferrite matrix with martensite islands, typically consists of holding the material in an austenite-ferrite (intercritical) regime followed by quenching and holding at temperatures slightly below the martensite start temperature

Figure 3

(a) Transverse sections of a DP steel with 0.147-wt% C, 0.403-wt% Si, and 1.868-wt% Mn, showing the microstructure evolution during hot rolling (*top*) and 75% cold rolling (*bottom*) for the sheet center (*left*) and the near-surface region (*right*). Examples of pronounced texture inhomogeneity in DP steels are determined by EBSD in transverse sections. (b) EBSD texture maps in IPF color coding taken over a region extending from the center to the surface of the hot-rolled sheet, revealing strong texture gradients. (c) Texture gradients through the hot-rolled sheet thickness in the form of preferred texture components (including 15° variation). (d) The most relevant texture components in terms of the orientation density $f(g)$ along the α -, γ -, ε -, and ξ -fibers that typically develop upon cold rolling (*orange*: surface layer; *dark blue*: center layer). Abbreviations: IPF, inverse pole figure; ND, normal direction; RD, rolling direction; TD, transverse direction. Adapted from Reference 41 with permission.

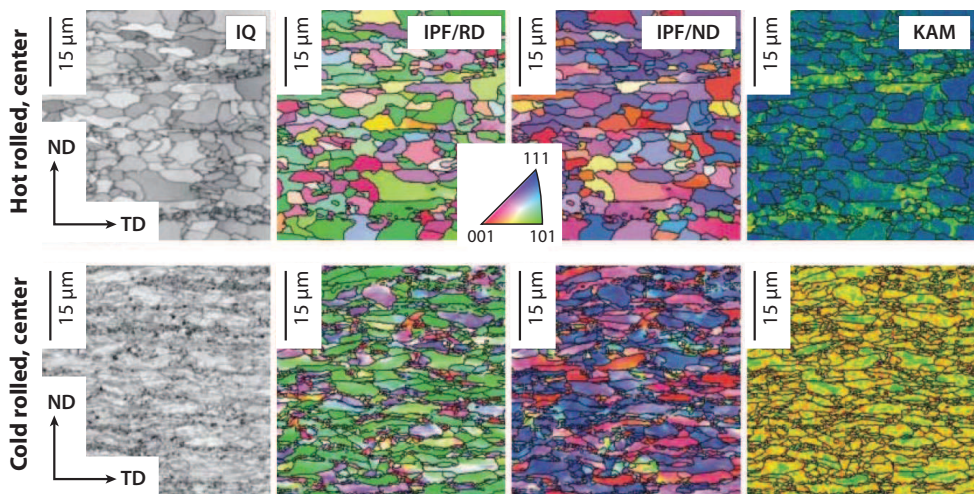


Figure 4

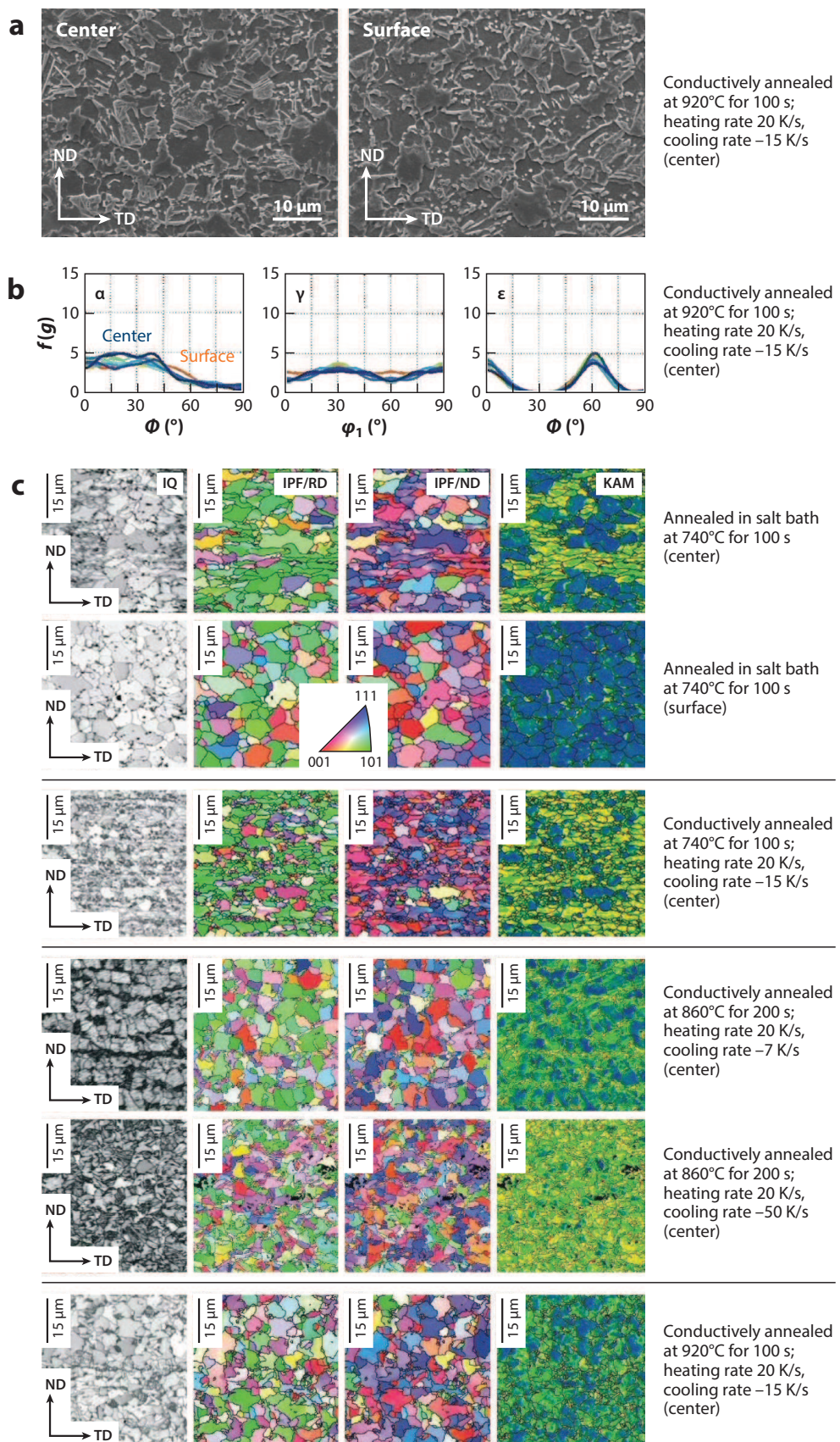
EBSD maps for the center of transverse sections of hot-rolled (*top*) and 75% cold-rolled (*bottom*) sheets of a DP steel with 0.147-wt% C, 0.403-wt% Si, and 1.868-wt% Mn. The microstructure is presented in terms of the IQ, IPF (IPF/RD and IPF/ND), and KAM (blue: KAM = 0°; red: KAM = 3°). Grain boundaries with angles larger than 3° are indicated by black lines in the IPF and KAM maps. Abbreviations: IPF, inverse pole figure; IQ, image quality; KAM, kernel average misorientation; ND, normal direction; RD, rolling direction; TD, transverse direction. Adapted from Reference 41 with permission.

(58–60) whereby the austenite fraction transforms into martensite (**Figure 2**). Another approach is quenching from the fully austenitic regime so that most of the undercooled austenite forms ferrite, whereas the remainder transforms into martensite. Targeted alloying, e.g., by minor additions of Cr and Mn, leads to the suppression of pearlite and bainite.

Depending on annealing temperature, time, and the preceding cold-rolling reduction, either phase transformation or recrystallization is the prevalent mechanism (40, 42–44). **Figure 5** summarizes microstructure trends associated with varying annealing temperatures, annealing times, and cooling rates. DP steel microstructures that were conductively annealed at 860°C and 920°C (i.e., close to A_{c3} and above A_{c3} , respectively; see **Figure 2**) for various times provide an overview

Figure 5

(*a*) SEM of transverse sections of fully processed DP sheets taken in the center (*left*) and at the surface layers (*right*) (composition 0.147-wt% C, 0.403-wt% Si, and 1.868-wt% Mn). Microstructure for samples conductively annealed for 100 s at 920°C and cooled at -15 K/s shows that only partial austenite-martensite transformation occurs, leading to a ferritic-martensitic microstructure. The morphology and distribution of the constituents are identical in the center and at the surface of the sheet. (*b*) Crystallographic texture fibers for the same conductive annealing conditions as a function of different through-thickness positions, revealing that the textures in all through-thickness layers become similar after annealing [*orange*: surface layer ($s = 0$) of the sheets; *dark blue*: center layer ($s = 1$) of the sheets]. (*c*) EBSD maps taken on transverse sections after various types of final heat treatments on a DP steel with 0.147-wt% C, 0.403-wt% Si, and 1.868-wt% Mn. For the 740°C salt bath heat treatment, center and surface microstructures are different. For the conductive heat treatments, the microstructures are similar through the thickness, and hence only the center layers are displayed. The images show, for each sample, the IQ, IPF/RD and IPF/ND, and KAM maps (*blue*: KAM = 0°; *red*: KAM = 3°) obtained from the same specimen area. Grain boundaries with angles larger than 3° are indicated by black lines in the IPF and KAM maps. Abbreviations: IPF, inverse pole figure; IQ, image quality; KAM, kernel average misorientation; ND, normal direction; RD, rolling direction; TD, transverse direction. Adapted from Reference 41 with permission.



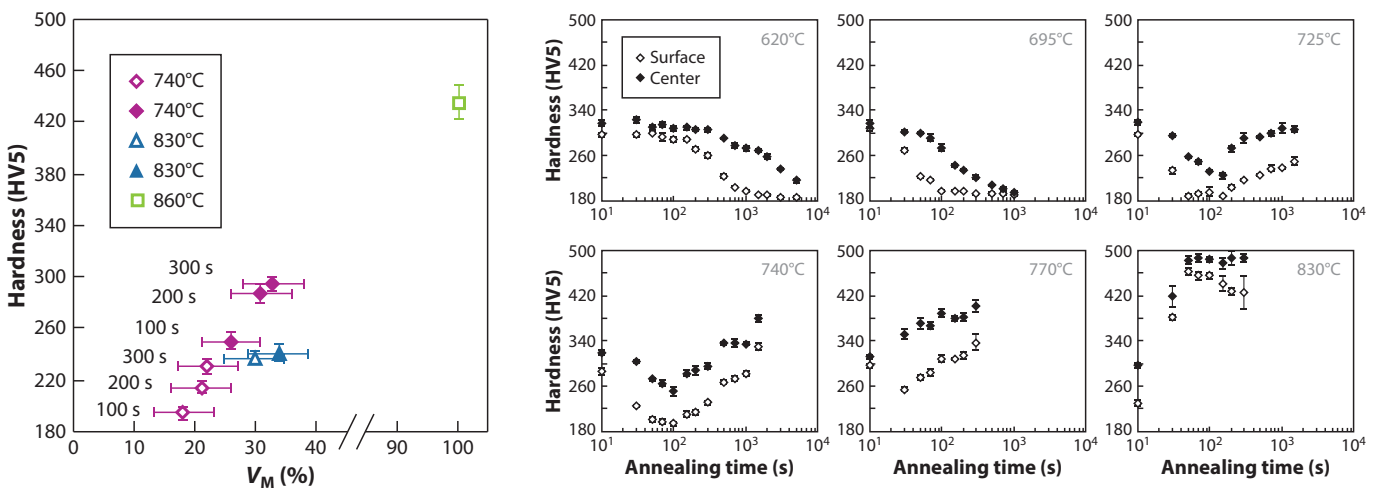


Figure 6

Evolution of the martensite volume fraction (V_M) and hardness for different salt bath annealing treatments after hot rolling and 75% cold rolling of a DP steel with 0.147-wt% C, 0.403-wt% Si, and 1.868-wt% Mn alloying content. The hardness evolution reflects the effects of ferrite recovery and recrystallization (softening) as well as the martensite volume fraction and its carbon content (hardening). At 620°C and 695°C, pronounced softening via recovery and recrystallization occurs. Hardening by martensite formation does not take place. At 725°C and 740°C, softening is observed for small annealing times, whereas longer heat treatments lead to transformation and thus to martensite-related hardening after quenching. This trend becomes more pronounced at 770°C. At 830°C, the hardness strongly increases due to massive transformation and martensite formation after quenching. Adapted from Reference 41 with permission.

of the effects of annealing temperature and time on microstructure evolution in the austenitic and near-austenitic temperature range (40, 41) (Figure 5).

2.3.1. Annealing in the austenitic phase field. To illustrate the effect of the heating rate, we include salt bath annealing (fast kinetics) and conductive heating (modest kinetics) of a DP steel alloyed with 0.147-wt% C, 0.403-wt% Si, and 1.868-wt% Mn (40–46, 56). For the case of rapid heating (salt bath), the hardness strongly increases from approximately 300 HV5 for cold-rolled sheets to values above 400 HV5 after 100 s (Figure 6). For longer annealing times, the hardness monotonically decreases to approximately 400 HV5. The microstructure for this reference case consists of pure martensite with isolated ferrite grains. For both annealing treatments, the martensite has an acicular morphology.

In specimens conductively annealed at 920°C and cooled at -15 K/s , only partial austenite-martensite transformation occurs, leading to a ferritic-martensitic microstructure (Figure 5). The martensite is heterogeneously distributed, with a volume fraction of 50–60%. The martensite and ferrite after such heat treatment are no longer arranged in the form of bands.

After austenite annealing, only low through-thickness texture inhomogeneity is found. That is, the strength of the crystallographic texture fibers does not substantially depend on the through-thickness position after cooling. The fractions of the texture components $\{001\}\langle\bar{1}\bar{1}0\rangle$ and $\{112\}\langle\bar{1}\bar{1}0\rangle$ of the α -fiber significantly decrease compared with those in the texture of cold-rolled material. The local orientation gradients within the ferrite grains strongly decrease after phase transformation (Figure 5). Ferrite is characterized by larger IQ values and smaller KAM values compared with the corresponding values for martensite (61). The KAM values within the ferrite grains typically increase close to ferrite-martensite interfaces. This increase can be explained by an increase in the dislocation density induced by the volume increase accompanying the austenite-martensite transformation (8) (Figure 5).

2.3.2. Annealing in the high intercritical temperature regime. High intercritical heat treatments [i.e., those conducted close to A_{c3} (**Figure 2**) by salt bath annealing at temperatures between 800°C and 850°C] yield concurrent recrystallization and phase transformation (1, 35–41, 56, 62). The morphologies observed by SEM after high IA are similar to those found in sheets annealed at a low IA temperature (e.g., 740°C) for the same model alloy (**Figure 5**). In the sheet centers, ferrite and martensite are aligned as bands along the rolling direction, whereas both constituents are more dispersed and heterogeneously distributed in near-surface regions.

2.3.3. Through-thickness texture and microstructure after annealing. When cold-rolled sheets are subjected to high intercritical or austenitic annealing temperatures, the developments of microstructure and texture and the resulting mechanical properties are dominated by phase transformation over recrystallization effects (**Figures 5 and 6**). Phase transformation leads to the formation of martensite and to new equiaxed ferrite grains with small in-grain orientation gradients.

Another effect associated with high annealing temperatures is a strong reduction in or even complete elimination of the inherited through-thickness texture inhomogeneity within short annealing times. The ferrite-martensite band structure in the center of the sheets typically reveals a stronger percolation after annealing at high compared with low IA temperatures. The microstructure exhibits a more homogeneous distribution of ferrite-martensite when subjected to austenitic annealing temperatures. In contrast, in specimens heat treated at lower temperatures, ferrite recrystallization prevails, and the inherited through-thickness texture and microstructure inhomogeneity, as well as the resulting mechanical gradients, are to some extent preserved (**Figures 5 and 6**).

2.4. Interaction Between Recrystallization, Diffusion, and Phase Transformation

When a cold-rolled ferrite-pearlite microstructure is heated to form an austenite-ferrite composite (which ultimately yields a DP microstructure after quenching), ferrite recovery and recrystallization, ferrite-to-austenite transformation, and carbon diffusion are relevant mechanisms (40, 54). As discussed above, these phenomena can occur consecutively or concurrently, depending on composition and on the imposed heating temperature, time, and rate. Especially at intermediate heating rates, complex interactions among the various nucleation, diffusion, growth, and transformation phenomena can occur (46, 52, 54, 56). Owing to the nonlinearity of the mechanisms involved, minor changes in these interactions can have a profound influence on the resulting microstructure. It is essential to quantitatively understand and evaluate the interdependence and competition among these metallurgical processes to arrive at a knowledge-based design of optimal process routes and microstructures.

2.4.1. Experimental observations of the interaction between recrystallization, phase transformation, and diffusion. Interactions between recrystallization and phase transformation were reported to occur for various types of cold-rolled and subsequently IA DP steels (40–44, 56) (**Figure 6**). Peranio et al. (40, 41) studied the influence of the driving force, heating rate, temperature, and holding time on the resulting DP steel microstructures and hardness for a steel with 0.147-wt% C, 0.403-wt% Si, and 1.868-wt% Mn. Recovery and recrystallization prevailed for annealing at ferritic temperatures and at (low) intercritical temperatures up to 740°C, at which the recrystallization time decreased with increasing annealing temperature and heating rate. The incubation and recrystallization times were smaller at the surface than at the center of the sheets, which was explained in terms of the larger deformation in the near-surface regions and the strong α -fiber texture components in the sheet center. Additionally, at annealing temperatures of 740°C, full recrystallization occurred at the surface, and only partial recrystallization occurred in the center. The volume fraction of recrystallized ferrite increased with increasing heating rates.

Depending on the Mn and C content, phase transformation starts in most DP steels above 700–710°C, and pure austenite prevails above 840–860°C (40, 41, 56) (**Figure 2**). The incubation time for phase transformation decreases with increasing annealing temperature. At austenitic temperatures, new equiaxed ferrite grains with low orientation gradients and different textures form. At low intercritical temperatures, ferrite and martensite typically exhibit the same spatial distribution as do ferrite and pearlite in the preceding cold-rolled material. This observation results from a microstructure memory effect due to pearlite regions undergoing phase transformation before ferrite (owing to the higher abundance of carbon from the cementite lamellae).

During austenitic annealing, ferrite and martensite are typically heterogeneously dispersed. V_M increases with annealing time until phase transformation is complete. Also, V_M increases with increasing cooling rate. Substantial overlap of recrystallization and phase transformation occur mainly at intermediate and high IA temperatures (**Figure 6**). At low IA temperatures, recrystallization and phase transformation proceed following distinct kinetics. Yang et al. (42) observed austenite nucleation both on grain boundaries of unrecrystallized ferrite and at the interfaces between recrystallized and unrecrystallized grains. The authors revealed an influence of ferrite recrystallization on the formation and dispersion of the austenite. Huang et al. (43) studied the effect of the initial heating rate on austenite formation and on ferrite recrystallization in two DP steels. They identified a strong interaction between ferrite recrystallization and austenite formation and suggested that this effect may alter the kinetics of austenite formation as well as the spatial distribution of austenite. Azizi-Alizamini et al. (44) confirmed these findings.

During IA, two different scenarios of austenite nucleation are usually discussed (54). The first one is austenite formation at ferrite-cementite interfaces within the carbon-containing (pearlite) colonies. The second one is nucleation at ferrite-ferrite grain boundaries. Nucleation of austenite often begins at pearlite colonies owing to the availability of carbon from the cementite. The newly formed austenite nuclei grow rapidly at the expense of the pearlite and subsequently of the surrounding ferrite. During this process, austenite growth is limited mainly by carbon diffusion inside the austenite.

Due to the surplus of carbon in pearlitic regions, the transformation proceeds much faster for those austenite zones that nucleate at the pearlite than for those formed at ferrite grain boundaries. In ferritic-pearlitic microstructures, austenite nuclei that form at ferrite-ferrite grain boundaries have no direct contact with a carbon source, such as cementite. In this case, the subsequent growth of the austenite nuclei requires carbon diffusion from the carbon-rich areas through the ferrite matrix to support the austenite formation at the moving austenite-ferrite interface. For the case of an initially ferritic-bainitic microstructure, a higher dispersion of carbon sources is typically present, supporting faster austenite formation.

At high IA temperatures, microstructure formation is governed by austenite transformation and depends critically on the annealing temperature and dispersion of the carbon sources. At low IA temperatures, ferrite recovery and recrystallization prevail. This process is also reflected by the mechanical properties of the material observed after quenching. As **Figure 6** shows, the hardness of martensite increases with the carbon content. In sheets annealed at high temperatures, diffusion leads to a more homogeneous carbon distribution and hence to a reduction in the average carbon content within the martensite. Another reason for the nonlinear increase in the steel's hardness as a function of V_M is that after annealing, the martensite can assume a granular morphology for IA and an acicular morphology for austenitic annealing.

2.4.2. Simulation of dual-phase steel heat treatment. The results reviewed above reveal that it is experimentally challenging to separate the individual metallurgical processes (e.g., recovery, recrystallization, diffusion, and phase transformation) occurring during heat treatment of DP steels.

Microstructure-based transformation models (63), such as cellular automata (CA), Monte Carlo (MC), and phase field methods, provide deeper insights into the mechanisms and morphological complexity associated with the interplay of phase transformations and recrystallization in DP steels.

Rudnizki et al. (46) developed a phase field model to describe the austenite formation from a ferrite-pearlite starting microstructure during annealing of cold-rolled DP steel. The simulation started from an already recrystallized microstructure. Hence, the approach did not consider the interaction between recrystallization and phase transformation. Zhu & Militzer (64) introduced a phase field model for the simulation of the microstructure evolution during IA of a DP steel. The study focused on the interaction between ferrite recrystallization and austenite formation, starting from a cold-rolled pearlite-ferrite microstructure for the case of high heating rates. The austenite-ferrite phase transformation was assumed to occur under conditions in which only carbon partitions between the phases via long-range diffusion. A solute drag model was implemented to describe the effect of substitutional alloying elements on the migration of the ferrite-austenite interface during the transformation. Bos et al. (47, 48) used a 3D CA model to describe the through-process microstructure evolution during the processing of DP steels. Here, these researchers considered both concurrent ferrite recrystallization and austenite formation, focusing on the influence of individual transformation processes on the DP microstructure. Interactions between recrystallization and phase transformation were not addressed. Okuda et al. (49) developed an MC model to simulate the competition between recrystallization and transformation in several DP microstructures, although the model lacked detailed thermodynamic criteria for the specific driving forces associated with either recrystallization or phase transformation. A more comprehensive model was introduced by Zheng and colleagues (54, 55), who used a 2D CA model to investigate the competition between ferrite recrystallization and austenitic transformation during the IA of cold-rolled DP steels. In this model, discrete microstructural constituents associated with both recrystallization and phase transformation are mapped through evolving thermodynamic criteria such as the stored deformation energy and the chemical driving force for transformation as well as kinetic effects such as grain boundary mobility and carbon diffusion. This comprehensive approach enabled a more quantitative microstructural prediction of material undergoing recrystallization and/or phase transformation. The model was used to study the influence of initial heating rate and annealing temperature on subsequent isothermal transformation kinetics and the associated microstructure evolution (**Figures 7** and **8**). Zheng & Raabe (54) also studied two types of scenarios for austenite nucleation, namely nucleation within pearlite, with its high carbon abundance, and nucleation at ferrite-ferrite grain boundaries, with a lower supply of carbon (see Section 2.4.1). The authors also considered the interaction of these scenarios with ferrite recrystallization.

In Zheng & Raabe's (54) simulation, the local chemical driving force acting on the moving heterointerface for the ferrite-to-austenite phase transformation was calculated in proportion to the deviation from the equilibrium concentration (65, 66) by using values from Thermo-Calc (<http://www.thermocalc.com/>) (**Figure 7a**). The pearlite was treated as an effective medium with an average carbon content of 0.71 wt% (i.e., the eutectoid carbon concentration). Nucleation of primary ferrite recrystallization was treated as a thermally activated process in conjunction with a continuous nucleation law (67), allowing the effects of both temperature and time dependence to be simulated. The driving force for ferrite recrystallization was taken as the difference between the stored deformation force and the particle pinning force (68–70).

The simulations show that the interactions between primary ferrite recrystallization, and the initial pearlite, affect not only the transformation kinetics (**Figure 8**), but also the morphology and spatial distribution of the austenite (**Figure 7**). Both ferrite recrystallization and phase transformation are significantly promoted by an increasing annealing temperature because they

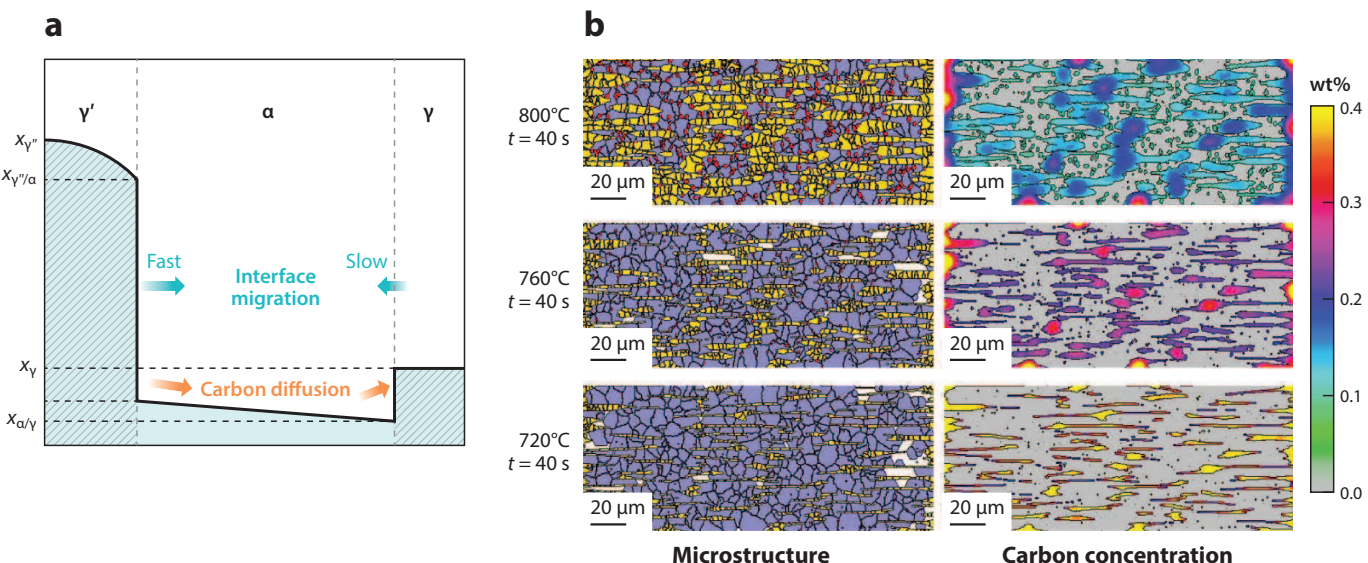


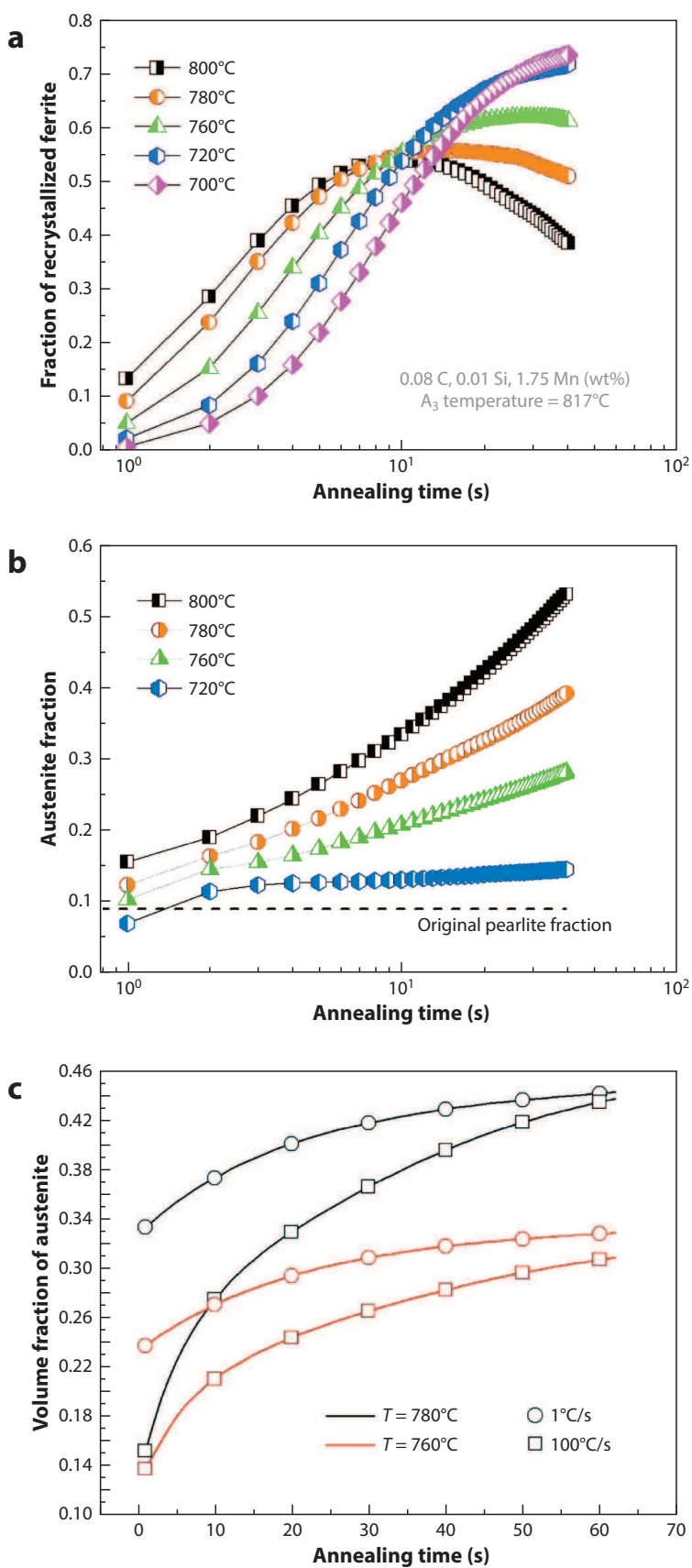
Figure 7

(a) Schematic of the variation in carbon content, x , across the austenite-ferrite boundary. γ' denotes pearlite-nucleated austenite, α denotes ferrite, and γ denotes grain boundary-nucleated austenite. The blue arrows indicate the direction of the austenite-ferrite interface migration, and the orange arrows indicate carbon diffusion. The austenite nucleating at former pearlitic regions (γ') has a very high nonequilibrium carbon content $x_{\gamma'}$ due to the dissolving cementite and hence grows very fast. The austenite nucleating at ferrite-ferrite grain boundaries requires carbon transport through the ferrite or along the grain boundaries and hence grows much slower. (b) Simulated microstructures (left) and corresponding carbon concentrations (in weight percent) (right) in the austenite phase after 40 s at three different IA temperatures ($A_3 = 817^\circ\text{C}$, as calculated by Thermo-Calc). The yellow areas denote the fast-growing pearlite-nucleated austenite regions, and the small red patches denote the slow-growing grain boundary-nucleated austenite zones. The blue regions indicate recrystallized ferrite, and the white zones indicate unrecrystallized ferrite. The black lines indicate grain boundaries. Adapted from Reference 54 with permission.

are kinetically closely related. Experimental temperature-dependent hardness data (Figure 6) confirm these predictions. Increasing the annealing temperature promoted the formation of austenite necklace structures along grain boundaries. Increasing heating rates produced a variety of fully to partially recrystallized microstructures prior to austenite formation, with a strong subsequent effect on austenite distribution. Increasing the initial heating rate promoted a morphology transition from a randomly distributed austenite structure to a banded austenite structure, in agreement with experiments.

Figure 8

(a,b) Simulated transformation kinetics of (a) ferrite recrystallization and (b) austenite formation during isothermal holding at various annealing temperatures. The kinetics shown in panel *a* and *b* reveal that at temperatures below 720°C ferrite recrystallization clearly prevails over phase transformation. Above 760°C, the volume fraction of ferrite is ultimately reduced by phase transformation, which starts to sweep the material for annealing times above 10 s. At 800°C, i.e., near A_3 , the transformation starts to substantially reduce the recrystallized ferrite volume fraction for annealing times above 10 s. In all cases, ferrite recrystallization proceeds much faster than the ferrite-to-austenite phase transformation. (c) Effect of initial heating rate on the kinetics of isothermal austenite formation during holding at 780°C and 760°C, respectively. Some of the associated microstructures are shown in Figure 7. The simulated material is a DP steel with 0.08-wt% C, 0.01-wt% Si, and 1.75-wt% Mn. The A_3 temperature, at which the ferrite-to-austenite transformation is completed, is 817°C, as calculated by Thermo-Calc. Adapted from Reference 54 with permission.



3. MECHANICAL BEHAVIOR AND DAMAGE OF DUAL-PHASE STEELS: EXPERIMENTAL OBSERVATIONS

3.1. General Characteristics

The main driver for the development of DP steels is their mechanical performance. Thus, most reports in the literature focus on their mechanical behavior. Rashid (71), in this journal's predecessor, described the mechanical characteristics of DP steels and provided a detailed overview of DP steel research through the 1980s. Section 3 of the present review provides an overview of the state-of-the-art understanding of the connection between the underlying microstructure and the resulting mechanical properties. We start by briefly revisiting the general property-microstructure trends and then discuss the complex micromechanics of DP steels. We emphasize those works that provide direct experimental observations of deformation mechanisms in ferrite and martensite, and the strain partitioning among them, as well as damage and failure mechanisms. Section 3.4 is devoted to the mechanical behavior of DP steels in the presence of hydrogen, which significantly affects damage and failure mechanisms and therefore limits the application of DP steels in some environments. We conclude Section 3 with an overview of the microstructure dependence of DP steel properties. The analyses presented below primarily cover quasi-static tensile loading, which constitutes the main body of DP steel literature, although other important studies in the literature focus on different loading conditions, e.g., cyclic loading (72).

The mechanical properties of ferrite-martensite DP steels are unique in comparison to those of other steels, as illustrated in **Figure 9**. Their composite soft-matrix/hard-reinforcement microstructure suggests that these steels would mechanically behave in a similar fashion as, e.g., ferrite-pearlite steels. However, as observed in **Figure 9**, DP steels exhibit early and continuous yielding, high initial strain-hardening rate, and high overall strength and ductility; Lüders bands

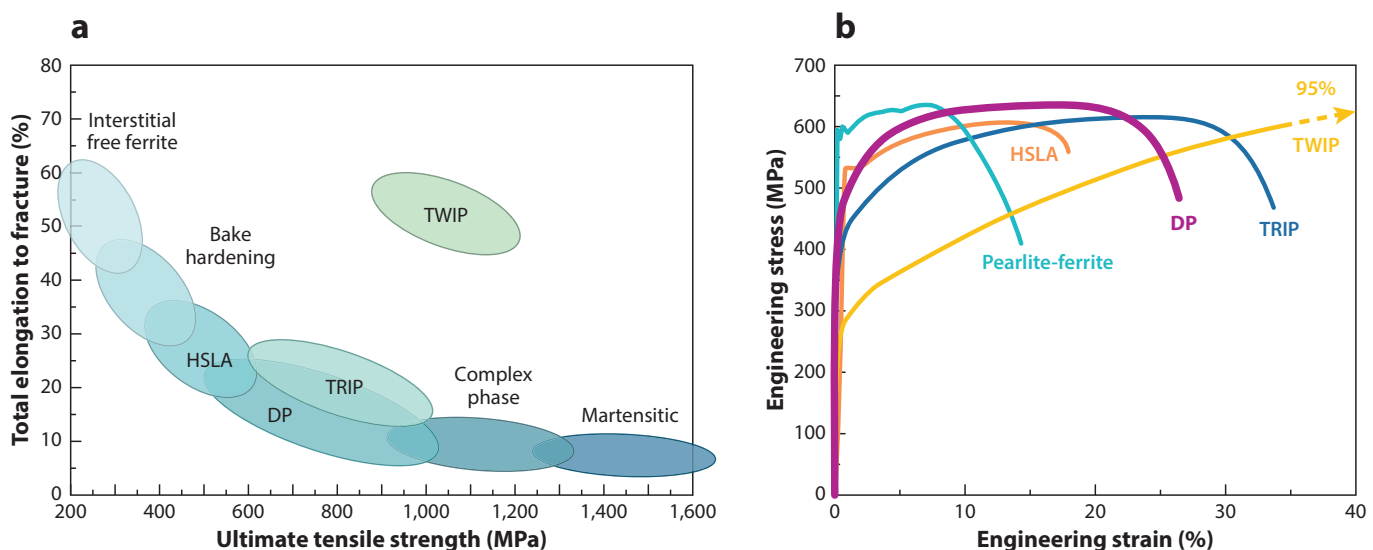


Figure 9

Comparison of the mechanical properties of DP steels with respect to other advanced high-strength steels. (a) Total elongation to failure versus ultimate tensile strength. (b) Quasi-static tensile stress-strain response at similar ultimate tensile strength levels for pearlite-ferrite steel, HSLA steel, DP steel (adapted from Reference 71 with permission), TRIP steel (adapted from Reference 73 with permission), and TWIP steel (adapted from Reference 74 with permission). Abbreviations: HSLA, high strength low alloyed; TRIP, transformation-induced plasticity; TWIP, twinning-induced plasticity.

are absent. The combination of early-stage yielding and high strain hardening is the basis for the excellent sheet-forming and component performance properties of these alloys for automotive applications, for which high formability is as important as the service properties. That said, there is significant room for improvement, especially for high-martensite DP steels, which are more prone to microstructural damage, as often measured in the industry via the hole expansion test. In fact, damage tolerance has been driving the design of other AHSSs [e.g., transformation-induced plasticity (TRIP) steels, quench-partition steels, and twinning-induced plasticity (TWIP) steels]. Although these more recent generation AHSSs have superior ductility compared with DP steels (**Figure 9**) while maintaining the strength levels of (or, in the case of TWIP steels, even having higher strength than) DP steels, they suffer from other practical issues (e.g., Mn segregation, high alloying costs, casting problems, difficulty in welding) and thus fall behind DP steels in automotive applications. There is thus a clear need to develop a deeper understanding of deformation mechanisms to guide novel strategies for highly damage-tolerant DP microstructures.

3.2. Deformation Mechanisms and Stress-Strain Partitioning

We now focus on the deformation mechanisms that lead to the mechanical behavior of DP steels shown in **Figure 9**. Multistage strain-hardening behavior was observed in early DP steel research (3). Thus, most subsequent experimental characterization efforts aimed at identifying the strain accommodation processes in ferrite and martensite at different stages of straining. This goal has been difficult to achieve for two reasons: Comparative analyses across different published reports are complicated by the large microstructural and composition parameter space of DP steels, and the microstructural localization (75) that is present even during a uniform deformation regime leads to great complexity in isolating the microstructural mechanisms of deformation and failure.

Nevertheless, several systematic analyses have been carried out. For example, Korzekwa et al. (3) studied the evolution of the ferrite dislocation substructure in DP steel on the basis of TEM investigations, paying special attention to the heterogeneity in the dislocation distribution. They observed a very low average dislocation density in the undeformed state far from the ferrite grain boundaries and a high dislocation density near the martensite-ferrite interfaces. In the initial stages of deformation (1–2% strain), planar dislocation walls and then incipient dislocation cells formed close to the martensite. At 7% strain, a dislocation cell structure with thick cell walls was observed, with smaller cell sizes closer to the martensite islands. At 14% strain, further thinning of the cell walls was observed, although such thinning was not accompanied by a further reduction in cell size. The corresponding stages of martensite plasticity, in contrast, are still not fully clarified. Because of the high initial dislocation density and the hierarchical substructure of martensite, plastic processes in martensite cannot be investigated as easily as those in ferrite.

In situ SEM investigations have been valuable in assessing the strain partitioning between ferrite and martensite, which was observed as early as 1986 by Shen et al. (76). In their work, they point to the heterogeneity of deformation in ferritic grains (on the basis of the distribution of slip steps) and to the fact that the straining of the two phases is not uniform but rather depends on different microstructural parameters, such as C_M and V_M , and on the level of tempering (76). Investigators recently demonstrated that direct information on strain partitioning can be obtained using in situ mechanical testing, which combines microstructural imaging during deformation and follow-up microscopic digital image correlation (μ DIC) analysis of the strain field (77–84). **Figure 10** shows three examples of strain map outputs of these various works. The rapid increase in the number of studies addressing local strain fields, accompanied by improvements in resolving capabilities and coupling to microstructure characterization (e.g., by EBSD), underscores the value of this methodology in understanding DP steel micromechanics.

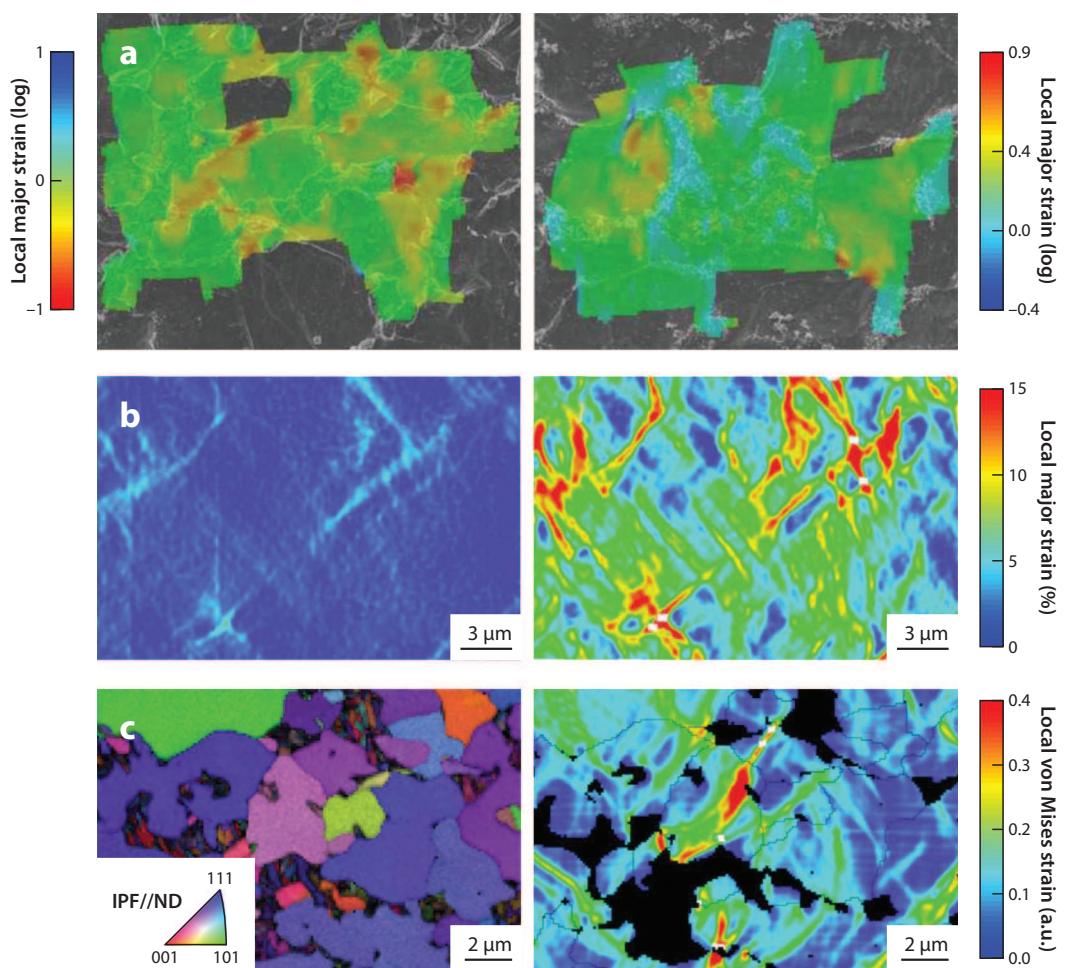


Figure 10

DIC analyses of DP steels adapted from (a) Reference 77, (b) Reference 81, and (c) Reference 84 with permission. The color codes represent either equivalent strain measures or individual strain tensor components, except for the EBSD-derived IPF maps from Reference 84. Abbreviations: IPF, inverse pole figure; ND, normal direction.

Employing *in situ* testing with DIC, Kang et al. (77) showed that strain partitioning between ferrite and martensite can be significantly decreased by a tempering treatment, leading to an increase in the critical damage nucleation strain (**Figure 10a**). Ghadbeigi et al. (79) presented a quantitative analysis of critical strain levels for different damage nucleation mechanisms in a DP1000 microstructure, reporting local strains well above 100% for damage initiation within ferrite and at martensite-ferrite phase boundaries. Tasan et al. (78) demonstrated that the detrimental influence of microstructural banding strongly depends on band continuity and morphology, as well as on the mechanical character of the constituent phase. Also focusing on a DP1000 steel, Kapp et al. (80) reported the severe heterogeneity of the strain distribution, which increases with increasing global deformation level. Deformation hot spots developed in ferrite channels between bulky martensite regions and at grain boundaries normal to the loading direction. Using an advanced pattern deposition technique to achieve higher strain resolution, Joo and coworkers (81) recently pointed out that the strain heterogeneity in DP steels is more complex than suggested earlier (**Figure 10b**). Marteau et al. (82), employing a microlithography-based pattern and EBSD-based microstructure

characterization, presented a detailed report on the role of different microstructural factors in strain heterogeneity. Their results suggest that the most critical factor causing strain heterogeneity is the local microstructural neighborhood rather than the specific grain orientation, shape, or size. These observations are also supported by a recent report by Han and coworkers (83). Tasan et al. (84) showed that plastic deformation in DP steels is distributed as a network with nodes, bands, and encapsulated regions (**Figure 10c**). The level of strain localization during loading was affected by the specific microstructure. For example, larger ferrite grains yield at lower load levels than do smaller ones in coarser DP microstructures and thus act as the nodes in the deformation network. In finer DP microstructures, in contrast, the strain and stress partitioning is more heterogeneous, and the size and dispersion of martensitic regions become more critical. For regions with well-dispersed martensite islands, more of the ferritic regions contribute to strain accommodation and hardening. For microstructures in which martensite is bulky, strain localization takes place at lower loads, possibly leading to earlier macroscopic strain localization. The authors also reported the importance of martensite morphology, especially for harder (i.e., high-carbon) martensite, as well as the unexpected degree of strain heterogeneity in ferrite, which relates to the in-grain microstructural heterogeneities from processing (75). In fact, high-resolution DIC measurements, coupled to EBSD measurements or microstructure simulations, reveal that the strain distribution in DP steels is much more heterogeneous than was originally proposed (75, 84). Although GND density gradients and elastic residual stresses clearly play a role in the observed intragranular strain heterogeneity, further investigations using the newly emerging techniques are warranted.

In addition to DIC-based full-field analyses, microtesting investigations were carried out, focusing on the deformation mechanisms in ferrite and martensite. Ghassemi-Armaki et al. (85) conducted one of the most systematic studies. They observed, by nanoindentation and micropillar compression tests, that the hardness across individual ferrite grains is not spatially homogeneous but is higher near the martensite-ferrite heterointerfaces. Interestingly, upon uniaxial loading, the harder ferrite on the grain perimeter softens, whereas the originally softer ferrite region in the grain interior hardens. Furthermore, the plastic deformation of martensite is triggered well before the UTS is reached.

From the results discussed in this subsection, we can infer that the plastic deformation in DP steels is triggered inside the soft ferrite regions and proceeds in a highly heterogeneous manner through the microstructure, affecting first the harder and spatially more confined ferrite regions and then the martensite. This heterogeneity arises due to strain partitioning between ferrite and martensite, as well as due to crystallographic or chemical heterogeneities within the ferrite. The level of strain partitioning, the contribution of martensite to strain accommodation, and the strains critical to nucleate damage strongly depend on microstructural parameters.

3.3. Damage Mechanisms

DP steels are prone to nucleating microcracks owing to the strain incompatibility of the martensite and ferrite phases and stress concentration due to morphological irregularities. However, microcracks can often be substantially blunted by localized deformation and hardening in ferrite, and thus DP steels do not fail in a catastrophic, brittle manner. Nevertheless, damage-induced softening plays a key role in the formability of DP steels, and significant effort is being applied to improving the understanding of these phenomena. The two challenges stated above for the analysis of deformation mechanisms also apply here: The relative activity of martensite cracking versus martensite-ferrite interface damage is strongly dependent on microstructural parameters (e.g., V_M) and on microstructural heterogeneity. Damage processes are dynamic, and thus a martensite cracking incident may resemble a martensite-ferrite decohesion incident due to

subsequent plastic deformation of the ferrite around the nucleated crack. Further complexity arises from the 3D nature of the damage initiation and growth. Here, X-ray microtomography can provide bulk information (86). However, to capture the initiation of damage, submicrometer probing, such as by field emission SEM, is required. One way to take 3D constraints into account at high resolution is by coupling SEM with 3D sectioning (75), although this approach is time intensive, even when automated focused ion beam techniques are used.

Impaired by the above-mentioned complexities, a variety of different damage mechanisms have been reported in DP steels. For example, Stevenson (87) and Mazinani & Poole (2) observed damage nucleation mainly in martensite islands, whereas Avramovic-Cingara et al. (88) investigated a DP600 steel and concluded that most failure initiation events are due to martensite-ferrite interface decohesion, nucleating perpendicular to the tensile axis and following ferrite grain boundaries. Avramovic-Cingara et al. (89) also reported more intense martensite cracking to be the main damage source when the martensite occurred in banded morphology, an observation confirmed by DIC analysis elsewhere (78). An earlier study by He et al. (90) on the influence of martensite morphology reveals that coarse microstructures are affected by martensite cracking, whereas decohesion prevails in finer microstructures. Given these disparate observations, a mechanism-oriented description of the role of microstructural features in damage nucleation, crack growth, and failure percolation is presently not available. **Figure 11** provides a detailed compilation of self-consistent observations of damage (2, 32, 36, 86, 88–100) in an effort to show the dependence of martensite cracking and martensite-ferrite decohesion on martensite fraction and ferrite grain size. If the martensite fraction is increased to a level at which martensite is fully connected, martensite exhibits plasticity earlier, and thus martensite cracking is promoted. In contrast, for large ferrite grain sizes and smaller martensite contents, interface damage mechanisms seem to be dominant. When ferrite grain size is decreased for low martensite fractions, both mechanisms are observed.

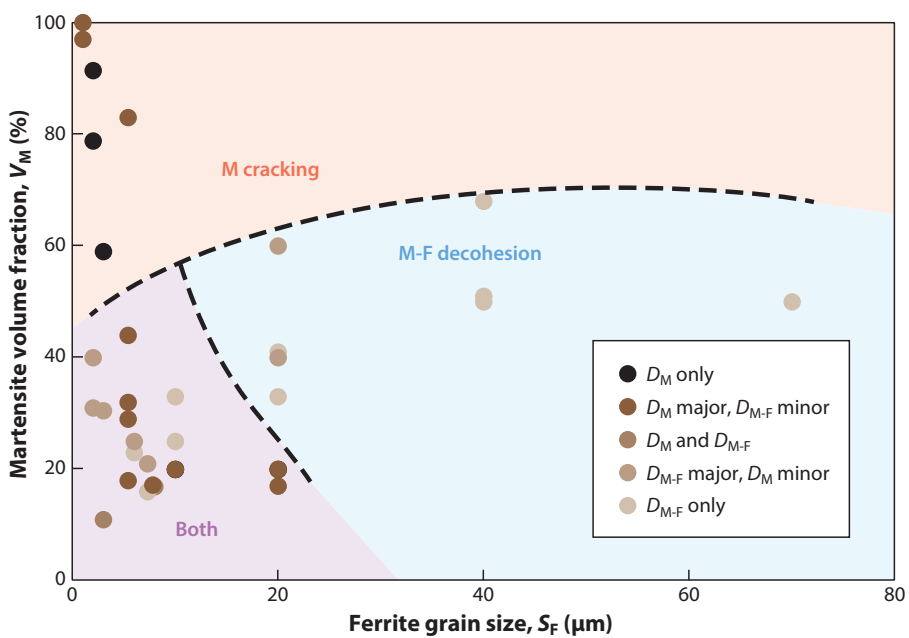


Figure 11

A compilation of damage mechanism analyses showing the effects of ferrite grain size S_F and martensite volume fraction V_M on the reported damage regimes: martensite cracking (D_M) and martensite-ferrite decohesion (D_{M-F}) (2, 32, 36, 86, 88–100). F and M indicate ferrite and martensite, respectively.

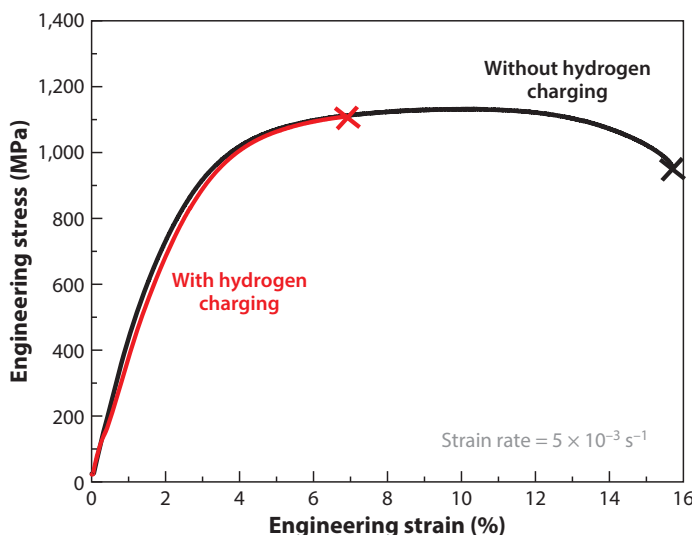


Figure 12

Engineering stress-strain curves of DP steel specimens with (red) and without (black) hydrogen charging, showing the effect of hydrogen on reducing ductility. Adapted from Reference 101 with permission.

3.4. Hydrogen Embrittlement of Dual-Phase Steels

Hydrogen embrittlement (HE) significantly deteriorates DP steel ductility, as **Figure 12** shows (101). Similar to the case for other high-strength steels, HE susceptibility of DP steels depends very strongly on the underlying microstructure, on the resulting strength, and on the hydrogen content (101, 102). Similar to damage mechanisms without the presence of hydrogen, HE susceptibility of DP steels can be associated with ferrite grain size (103), with martensite fraction (103), and with the internal structure of the martensite [e.g., the tempering condition (102) and carbon content (103)]. A comprehensive understanding of the HE micromechanics clearly cannot be achieved through an investigation of macromechanical analysis alone.

From the viewpoint of the microstructural factors, Davies (103) reported that HE susceptibility of DP steels increases with increasing martensite content, substantially increasing when the V_M exceeds 10 vol% and becoming constant above 30 vol%. According to Davies, the V_M dependence originates from damage propagation behavior associated with martensite cracking. Critical hydrogen content for the occurrence of HE is another important criterion with which to evaluate HE susceptibility. Toji et al. (104) reported that the hydrogen-related delayed fracture of DP steels can be assessed quantitatively in terms of diffusible hydrogen content, equivalent strain, and stress. The amount and distribution of hydrogen depend on stress state and plastic strain. Thus, the critical diffusible hydrogen content for hydrogen-induced delayed fracture should always be coupled with applied stress and strain, particularly given the inhomogeneous damage and strain distributions in DP steels.

To understand the underlying HE mechanism, Koyama et al. (101) carried out a detailed analysis for DP steel with and without hydrogen. **Figure 13a** shows average damage area plotted against local plastic strain with and without hydrogen charging. The damage evolution stages are classified into three regimes: incubation, nucleation, and growth. The incubation regime is completed when a damage incident is initiated at, e.g., a prior austenite grain boundary (see **Figure 13b**).

In the damage nucleation regime, the crack size is maintained due to crack arrest in ferrite, and a new damage incident nucleates in martensite (**Figure 13c**). Upon further deformation, the damage incidents start to grow (i.e., the damage growth regime) across ferrite and ferrite-martensite

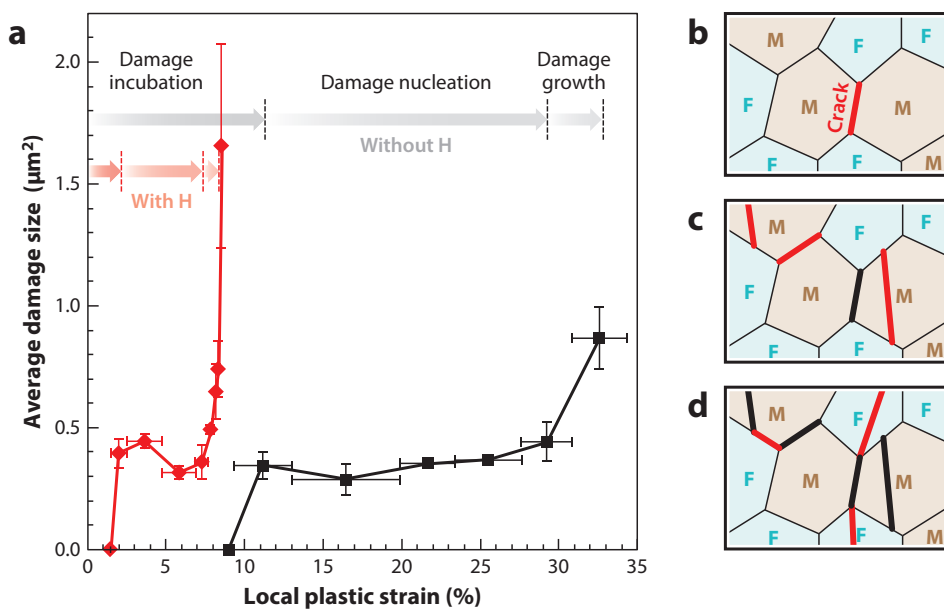


Figure 13

(a) Average damage area plotted against local plastic strain with (red) and without (black) hydrogen charging. The total elongations of the specimens with and without hydrogen were 6% and 12%, respectively. (b–d) Schematic illustrations of the damage evolution process corresponding to (b) the end of the damage incubation regime, (c) the damage nucleation regime, and (d) the damage growth regime. F and M indicate ferrite and martensite, respectively. The thick red lines indicate newly formed or propagated damage since the previous stage. Adapted from Reference 101 with permission.

interfaces until void coalescence and macroscopic failure (Figure 13d). Figure 13a shows that hydrogen reduces the resistance against crack initiation in martensite-related microstructure and deteriorates the crack arrest property in ferrite (due to the enhanced localized plasticity in the ferrite). These two characteristics promote the coalescence and propagation of damage, causing the distinct reduction in elongation shown in Figure 12.

3.5. Microstructure Dependence of Mechanical Properties

The UTS and elongation-to-failure values of all DP steels considered in this article are plotted in Figure 14 (1, 4, 37, 61, 98, 99, 105–114). The underlying complexity of DP steel microstructures makes direct comparisons across the different experimental studies difficult. Nevertheless, relying on comparisons of various publications, one can identify several trends. An increase in V_M or C_M increases strength but reduces ductility, whereas grain refinement simultaneously increases both V_M and C_M . Although only limited data are available, refinement of the martensite (when all other factors are kept constant) also seems to benefit ductility.

One of the few studies to provide detailed discussion of these trends is the experimental-numerical approach of Pierman et al. (116), who systematically investigated the three most critical microscopic parameters, namely V_M , C_M , and the microstructure morphology. They observed that a larger V_M increased both the yield and tensile strengths (due to the composite effect, with little contribution from ferrite strain hardening). Also, a higher C_M increased the strain hardening and tensile strength but did not affect the initial yield point. Ductility increased with V_M (for fixed C_M) and with C_M (for fixed V_M). Furthermore, equiaxed microstructures resulted in higher strength and lower ductility compared with specimens with finely dispersed elongated particles.

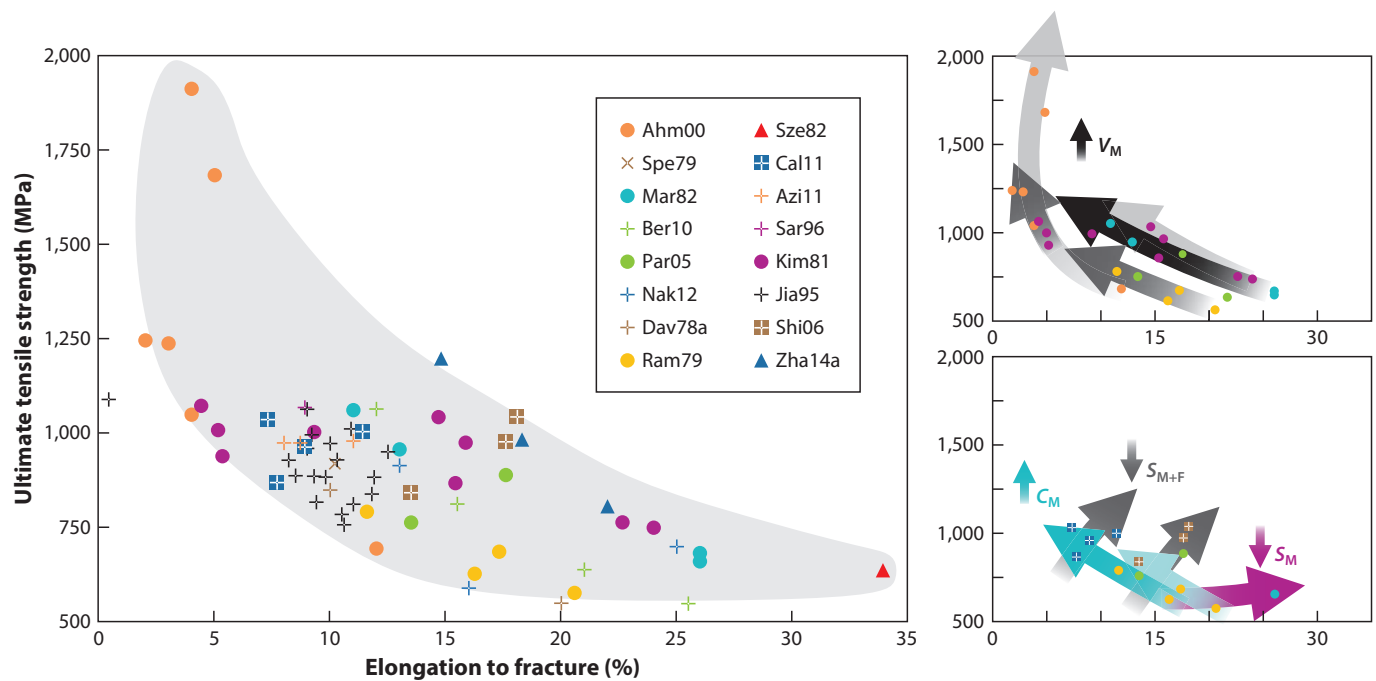


Figure 14

The UTS-ETF combinations of all DP steels reviewed in this article: Ahm00, Reference 106; Spe79, Reference 1; Mar82, Reference 105; Ber10, Reference 108; Par05, Reference 111; Nak12, Reference 110; Dav78a, Reference 109; Ram79, Reference 4; Sze82, Reference 114; Cal11, Reference 61; Azi11, Reference 107; Sar96, Reference 99; Kim81, Reference 98; Jia95, Reference 37; Shi06, Reference 112; Zha14a, Reference 113. Several trends due to microstructure effects are plotted on the diagrams to the right, where different arrows correspond to different individual studies. Abbreviations: C_M , martensite carbon content; S_{M+F} , martensite and ferrite grain size; S_M , martensite grain size; V_M , martensite volume fraction.

3.6. Novel Strategies for Dual-Phase Steel Property Enhancement

Some novel strategies have the potential to push the mechanical behavior of DP steel beyond the limits shown in **Figure 14**. They can be classified into three groups: (a) constitution modification, (b) phase morphology optimization, and (c) microstructure refinement. Here we briefly mention the former two and discuss the last in more detail.

The introduction of alternative phases, such as retained austenite or bainite, would obviously change the behavior of DP steels (**Figure 9**), although it is debatable whether steels with multiple new phases [e.g., the Quadplex steel with 1.3% carbon (115)] fall into the category of DP steels. In a recent study on the influence of a relatively minor change in the constitution, Maresca et al. (117, 118) showed that martensite plasticity can be strongly influenced by retained interlath austenite films as thin as a few tens of nanometers, even when the films are discontinuous. A careful measurement of the retained austenite film content in the martensite islands requires dedicated TEM analyses and is thus often not carried out. However, this study demonstrated the positive influence of austenite films, indicating a pathway for future DP steel variants with increased martensite toughness. The strength of this design strategy had been previously demonstrated for different steels (17, 119).

By optimizing ferrite and martensite morphology, stress state-optimized microstructures can be tailored. Two examples are based on accumulative roll bonding (113), although multilayered DP steel microstructures can also be produced by traditional thermomechanical processing routes.

Other examples in this direction are the formation of a bimodal ferrite grain size distribution (120) and DP steel microstructures with martensite islands of graded hardness (121).

Among the various strengthening mechanisms, grain refinement is unique in that it can simultaneously improve the toughness. Thus, its potential for DP steels is well studied (37, 122–126). Earlier studies discussed the nature of the Hall-Petch relationship in DP steels. For example, Chang & Preban (122) reported that the yield ratio increases with decreasing grain size. Jiang et al. (37) carried out a detailed analysis of the Hall-Petch correspondence and observed its slope to be larger for tensile strength than for yield strength. Through the use of an Ashby-type strain-hardening model, the more pronounced strengthening effect of grain refinement at low strains is attributed to the rapidly increasing density of GNDs. When the grain size is reduced, the ferrite-martensite boundary area fraction is increased, thus increasing the contribution of GNDs to the stress increment. At higher strains, in contrast, martensite starts to deform plastically, and the main strengthening contribution stems from statistically stored dislocations (SSD), whose density is independent of grain size.

Ultrafine-grained (UFG) refinement of DP steels has been investigated in the last decade and has shown promising results, as observed in **Figure 15** (8, 27, 61, 127–129). UFG DP steels with a S_F of approximately 1 μm have been produced via a two-step route consisting of (*a*) a deformation treatment to produce UFG ferrite and finely dispersed cementite or pearlite and (*b*) a short IA in the ferrite-austenite two-phase field followed by quenching to transform all austenite into martensite. Grain refinement in step *a* was achieved by equal-channel angular pressing (111, 123), cold rolling (110, 124), accumulative roll bonding (130), and cold swaging (125). Mukherjee et al. (126) proposed a single-pass processing route based on deformation-induced ferrite transformation. More recently, UFG DP steels were successfully produced by thermomechanical processing involving the consecutive steps of hot deformation, large-strain warm deformation, warm annealing, and IA (8, 27, 61, 127–129). Azizi-Alizamini et al. (107) produced UFG DP steels by rapid IA of fine ferrite-carbide aggregates.

Grain refinement of DP steels down to the UFG regime leads to increases in both yield strength and tensile strength, following a Hall-Petch-type linear relationship, whereas uniform elongation and total elongation are hardly affected (61, 123). Toughness is improved by grain refinement, as evidenced by a lower ductile-to-brittle transition temperature and an increase in both upper and lower shelf energies (129). The increase in the initial strain-hardening rate due to grain refinement is attributed to early dislocation interactions, to the high number of dislocation sources, and to the back stresses exerted by martensite particles and very small ferrite grains ($S_F < 1 \mu\text{m}$).

The plastic constraints in fine-grained and UFG ferrite force martensite to plastically deform at lower strains during tensile loading, whereas strain localization and subgrain formation are impeded. The increase in strength at improved ductility due to grain refinement (**Figure 15**) is attributed to the combined effect of strengthened ferrite and enhanced martensite toughness. In situ experiments and CP simulations have confirmed that the martensite toughening arises from spherical martensite islands free of stress-intensified, crack-prone regions (84).

4. MECHANICAL BEHAVIOR OF DUAL-PHASE STEELS: COMPUTATIONAL MODELING

This section presents theoretical and numerical approaches to describe the mechanical behavior of DP steels at different length scales. Analytical concepts and numerical tools to predict the mechanical behavior of two-phase materials were applied to the specific case of DP steel as early as 1974 (131). The number of published works has increased steadily since, accelerating during the last 5 years. On the engineering side, the high interest in simulating DP micromechanics and

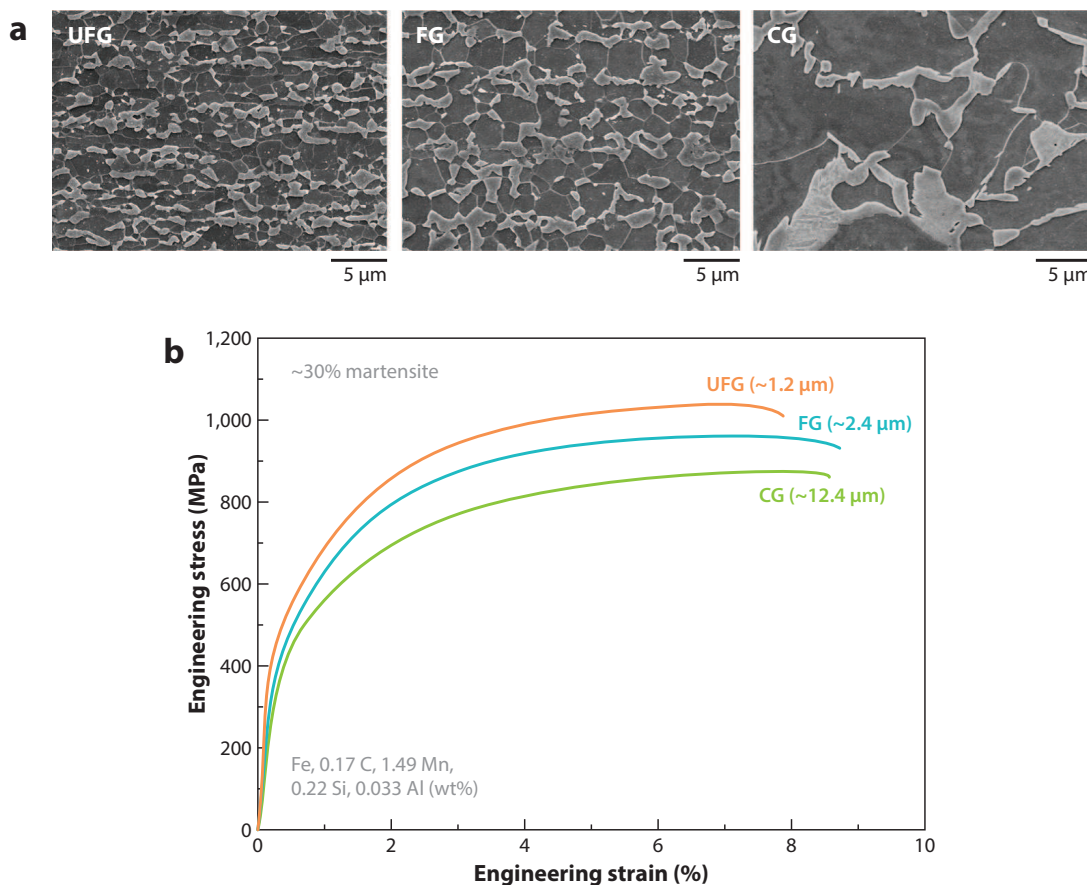


Figure 15

(a) Ferrite grain refinement from a conventional grain (CG) size ($S_F \sim 12.4 \mu\text{m}$) to fine grained (FG) ($S_F \sim 2.4 \mu\text{m}$) to ultrafine grained (UFG) ($S_F \sim 1.2 \mu\text{m}$) in a Fe-0.17C-1.49Mn-0.22Si-0.033Al DP steel ($V_M = 30\%$). (b) Improvements in the properties as a result of grain refinement. Adapted from Reference 61 with permission.

macroscale flow response is fueled by the requirement to adequately predict the material's behavior when exposed to sheet forming and crash loading. On the micromechanical side, the interest derives from the substantial challenges with modeling high-mechanical-contrast composite materials (e.g., elastoplastic codeformation of phases, mechanics of interfaces, size effects, and damage).

Supplementing and scrutinizing experimental results with complementary simulations provide crucial information not readily available from experiments (e.g., local stress fields at interfaces, early-stage damage initiation, and dislocation densities). Such an approach also enables systematic feasibility studies on model systems with respect to phase properties, V_M , phase percolation, interface property design, or texture.

One way to classify the approaches to examining the influence of microstructure on mechanical properties of DP steels is to assess the aim and the scale of the simulation. As illustrated in Figure 16, the works reviewed here fall into three categories (132, 133). First, predictions of the performance of structural parts and critical manufacturing steps are conducted using averaged material properties. Such component-scale simulations are reviewed in Section 4.1, focusing mainly on sheet metal-forming operations. Second, early reports on modeling DP steel mechanics targeted the prediction of the material's global response, typically stress-strain curves and strain-hardening characteristics, as a function of the underlying microstructural features and

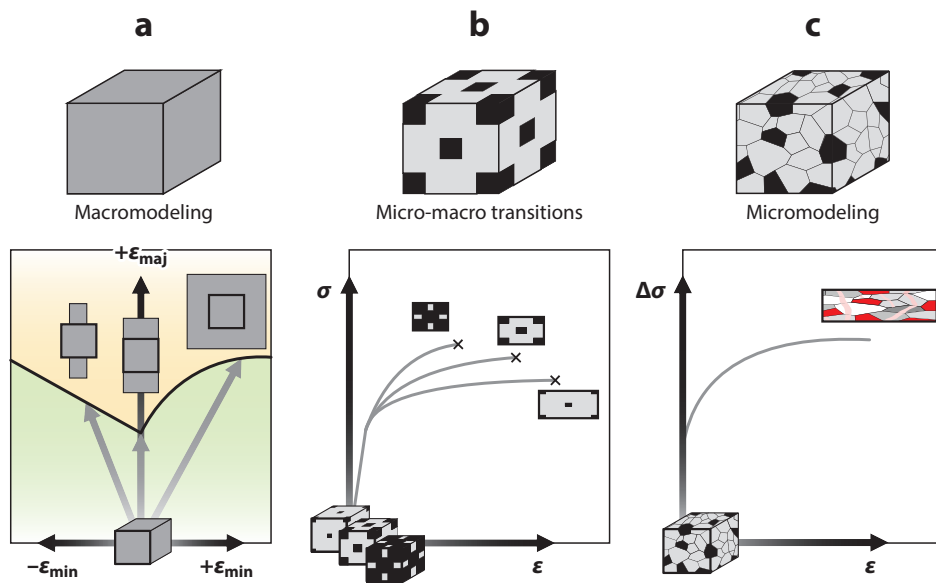


Figure 16

Classification of the three modeling regimes discussed in text. (a) Macromodeling at the component scale. On the basis of averaged yield surface and damage models, different sheet-forming regimes can be more (yellow) or less (green) prone to failure, as summarized in a forming limit diagram. (b) Micro-macromodeling aims at predicting flow curves and strain-hardening characteristics by using representative volume element methods. (c) Texture- and microstructure-informed full-field micromodeling to investigate micromechanics. This schematic shows the stress distribution between martensite and ferrite.

inherited textures. Section 4.2 reviews these efforts to bridge the microscopic and the macroscopic scales. Third, simulations addressing the local mechanical response of DP steels are presented in Section 4.3. At this scale, the physical and microscopic origin for the behavior of DP steels is examined. Whereas phase contrast is usually considered (Section 4.3.1), second-order effects, such as orientation, interface properties, and in-phase/in-grain gradients, are examined only in more recent works (Section 4.3.2).

4.1. Macromodeling

Component-scale simulations of DP steel (e.g., forming simulations) usually omit the crystalline nature of ferrite and martensite to decrease computation time while aiming to predict certain metal-forming and crash-relevant properties such as strain hardening and forming limits. A suitable description of the average material response is typically based on the concept of a yield surface. The simple von Mises isotropic yield surface is applicable only for weakly textured materials. A study by Huh et al. (134) on the effect of strain rate on yielding anisotropy compared three different yield descriptions. Wang et al. (135) compared the capabilities of different yielding models (the fourfold anisotropic Hill-48 and the more complex Barlat-89 and Banabic-2005 yield surfaces) in describing certain averaged directional properties of DP steels.

To compare simulated predictions with experiments, Lim et al. (136) assumed isotropic yielding and a Hollomon hardening law to simulate the elastic springback of DP steels subjected to sheet metal-forming operations. Tarigopula et al. (137) also used an isotropic yield surface, but with Voce hardening to complement low-, medium-, and high-strain-rate tests. Qin et al. (138) presented similar work on high strain rates, using a Johnson-Cook flow model to describe

strain hardening. Banu et al. (139) successfully applied the quadratic Hill-48 formulation, in combination with a Swift law for isotropic and kinematic hardening, to rail stamping. The same yield description was used by Chen & Koç (140) to simulate springback and by Firat (141) to predict necking on the basis of diffuse (Swift) or localized (Hill) criteria. Tarigopula et al. (142) presented an approach of fitting parameters for yield surface approximation and constitutive laws to measured data. The constitutive model includes isotropic and kinematic hardening. Galantucci & Tricarico (143) presented a thermomechanically coupled rolling simulation in which the use of a plain material model allows to take thermal effects into account.

4.1.1. Modeling damage, failure, and fracture. Prediction of forming limits is important when complex sheet-forming operations are optimized with respect to the yielding and stretching capacity of DP steel. Here we review models in which damage evolution was explicitly implemented into the forming simulations.

Gruben et al. (144) used a Voce-type hardening law fitted to experimental data and included damage-induced softening to examine crack propagation under different loading conditions predicted by various fracture criteria. Similarly, Tarigopula et al. (145) studied fracture in a shear test and compared the findings with experimental results obtained by DIC at a resolution above the grain size. Instead of using a shear test, Kim et al. (146) reported how a displacement-controlled draw-bending test was developed, carried out, and simulated using a constitutive law that accounts for thermomechanical effects, which are claimed to be important for the prediction of shear failure. However, fracture was not explicitly modeled in this approach.

These three studies used an isotropic hardening model, in contrast to the investigation of shear fracture conducted by Luo & Wierzbicki (147), in which the Hill-48 orthotropic yield surface was applied to simulate a coupled stretch-bending operation on DP steel. A modified phenomenological Mohr-Coulomb ductile fracture criterion was adopted to analyze the failure behavior. Lian et al. (148) presented damage modeling of a Nakajima test. Hu et al. (149) presented an experimental study of cyclic loading of DP (and TRIP) steels and a model derived to predict failure.

4.1.2. Multiscale and representative volume element models. Multiscale simulations aim to directly communicate information obtained at the microstructural scale to large-scale simulation while avoiding the main drawback of direct microstructural descriptions at a large scale, namely long computation times. Several approaches have been successfully implemented in multiscale modeling of DP steels. The relaxed grain cluster scheme is a finite-strain variant of the widely used grain interaction model (150). Roters et al. (151) reported an application of this model to cup drawing of DP steels. Although the application of multiscale finite element (FE^2) methods to DP steels gained momentum in recent years, the additional step of generating simpler representative volume elements (RVEs) is often intricate. Schröder et al. (152) presented corresponding work on RVE generation and simulations. A weak coupling in the spirit of FE^2 methods is also possible. In this approach, the loading for the small-scale model is determined from the results obtained from a respective large-scale simulation. For example, the boundary conditions for an RVE model were determined from a hole expansion simulation by Uthaisangsuk et al. (153) to investigate stretch flangeability, which is an important parameter for evaluating certain complex sheet metal-forming operations. Prawoto et al. (154) used the same concept, also incorporating damage modeling, for the simulation of impact loading.

4.2. Micro-Macro Transition

The high mechanical contrast between the soft ferritic and the hard martensitic phases is the reason for the gap between the upper and lower bounds of simple analytical isostrain and isostress

assumptions used for DP steel properties (155). Therefore, more sophisticated models are required to predict the global behavior of DP steels. The homogenization approach introduced by Mileiko (156) for fiber-reinforced composites has been adapted to DP steels by Davies (5) and Korzekwa et al. (157). Mori & Tanaka (158) developed a widely used Eshelby-type composite model.

As outlined in the early reviews on DP steels of Karlsson & Sundström (131) and Tomota & Tamura (159), these generic building block-type approaches are usually derived from somewhat unrealistic assumptions regarding the nonlinear phase and interface constitutive response and thus typically fail to reproduce the underlying microscale mechanisms in metallic composite materials loaded into the plastic regime. Hence, improved models for DP metals have been developed (160, 161), yielding better results, as shown by Bhadeshia & Edmonds (162) and Szewczyk & Gurland (114). On the basis of theoretical considerations and fitting to experimental data, a variety of expressions were developed to deal with the influence of grain size and V_M (122), retained austenite (163), and certain features of the strain-hardening behavior of DP steels (164, 165).

With growing understanding of DP micromechanics, the complexity of models for the prediction of the global response has also increased. For example, Bouaziz et al. (166) and Delincé et al. (125) presented simulation studies capable of predicting larger sets of DP flow curves for various phase fractions and carbon contents. Yoshida et al. (167), Tsuchida et al. (168), and Pierman et al. (116) recently published similar works.

4.2.1. Real microstructures. Even though Karlsson & Sundström (131) and Tomota & Tamura (159) showed that finite element analysis could be used to examine local micromechanical phenomena, the determination of global properties was the main aim in their studies. In these early works, the constitutive models remained simple. For example, an isotropic response was assumed for both elastic and plastic regimes. More recent formulations, such as dislocation density-based constitutive models (169), introduced internal variables, placing their focus on computing the macroscopic response resulting from different types of microstructures. Marvi-Mashhadi et al. (170) used a Voce-type hardening law with starting microstructures obtained from SEM images to simulate flow curves dependent on martensite content. Dong et al. (171) and Ramazani et al. (172) published similar works, investigating both local mechanical fields and the resulting global response.

A major drawback of using real microstructures for the determination of global properties is the limited size of the material probed. A comparison of the early work of Karlsson & Sundström (131) with recent results by Ramazani et al. (172) shows the drastic improvement in microstructure domain size and resolution. However, these simulations are still done in 2D to decrease computation time and, more importantly, because 3D data of real DP microstructures are hard to obtain (8, 173). These reasons promoted the use of idealized instead of real microstructures for the determination of global mechanical properties. Real microstructures, in conjunction with refined constitutive models, were reserved for micromechanical studies (see Section 4.3) (**Figure 17**). We anticipate that similar approaches will continue to gain momentum and help elucidate load concentrations and damage mechanisms in DP steels.

4.2.2. Idealized microstructures. To avoid the computational expense of using real microstructures to simulate average mechanical response, statistical models capturing key geometrical features in idealized (RVE) microstructures have been used in simulations. These simulations include investigations of phenomena such as the influence of individual phase properties on the average material response. This approach is effective as long as the local phase morphology does not play a substantial role in strain localization.

Liedl et al. (174) provided an early example of how idealized models can answer a specific question. These researchers investigated the micromechanical reasons for the dependency of work

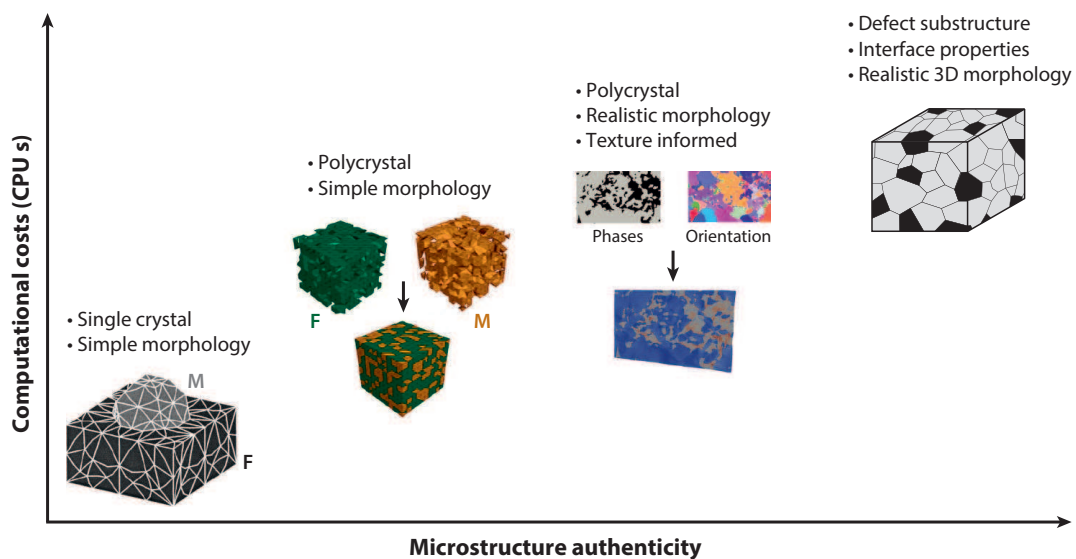


Figure 17

Correlation between computational costs and microstructural authenticity of the models: Progress in computational approaches enables more and more microstructural features to be taken into account, although doing so often leads to an increase in computational costs. F denotes ferrite, and M denotes martensite. The panel at the bottom left is adapted with permission from Reference 174, and the second panel from the left is adapted with permission from Reference 153.

hardening on martensite content with the help of a small-cell array using periodic boundary conditions. Asgari et al. (175) used a similar framework, although one based on a 2D microstructure. In these works, the results were compared with those obtained on real microstructures. Using a similar, plastically isotropic (J_2) material model, Al-Abbasi & Nemes (155) extended the use of simple geometries with the stacked hexagonal array model of Tvergaard (176). This model allows for the exploitation of symmetries to reduce computation time. The arrangement of hard, spherical/cube-shaped inclusions was further investigated in References 177 and 178. Uthaisangsuk et al. (153) used a more realistic, irregular, and simplified phase morphology with variable volume fractions of martensite. A direct application of the obtained average deformation parameters for modeling on the component scale is given in References 178 and 179. To account for the gradient in GND density, Kadkhodapour et al. (180) enhanced a simple inclusion model by introducing layers having different material properties in the ferrite surrounding the martensite island to study the effect of phase transformation-induced strain hardening.

4.3. Micromechanical Modeling

The aim of micromechanical simulations is to obtain a better understanding of the deformation mechanisms at the (sub)grain scale. Here, we discuss only simulations dealing with real microstructures as determined usually by SEM. Geometrically dominated building block-type models, in which the material model is kept simple (for example, stress and strain partitioning as a result of the contrast between martensite and ferrite only), are discussed first, followed by mechanism-oriented studies that build on more complex material models. In contrast to RVE modeling, micromechanical full-field simulations capture the extremes and patterns in the respective field quantities at the subgrain level rather than focusing on the average material response.

4.3.1. Geometry-dominated model. The phase contrast between ferrite and martensite is the most relevant feature in DP steel microstructures. Therefore, understanding effects associated with the complex shape of the martensite observed in real structures, including how it determines the interaction with the ferritic matrix, is of great importance. Sun et al. (181) investigated failure events in microstructures obtained from SEM images by using an isotropic yield description. Strain hardening was phenomenologically described by a Ludwik equation. Damage was modeled by introducing voids, and Sun et al. concluded that the ductility of ferrite and the existence of microvoids do not significantly affect the ductility of the DP steel. Similar work was done by Ramazani et al. (172), who investigated the influence of parameters such as V_M and S_M . Sodjit & Uthaisangsuk (182) considered the GNDs at the phase boundaries, as previously suggested by Kadkhodapour et al. (183). In a further development, Paul (179) used an isotropic, dislocation density-based formulation. Because no damage model was included, failure was predicted on the basis of a maximum plastic strain criterion. In the last four works discussed (172, 179, 181, 182), a direct connection to experimentally obtained local fields was not given, and only the average response obtained from experiments was compared with the computed results.

4.3.2. Mechanism-oriented models. Full-field micromechanical simulations are performed with the aim of an in-depth understanding of DP microstructures. Hence, their fidelity improves as more of the underlying physical mechanisms are incorporated. Textures, morphologies, constitutive strain-hardening details, damage models, void formation, and through-process inherited microstructures are examples of effects that matter at this scale. This subsection presents modeling studies of DP behavior at the grain level. In contrast to Section 4.3.1, consideration is given to the phase contrast between martensite and ferrite. The additional constitutive effects are incorporated either by using CP formulations to correctly model the anisotropic crystalline deformation modes or by adding models for damage.

Choi et al. (184) revealed that incorporation of crystallographic orientations into DP steel micromechanics is important, even though the mechanical contrast between ferrite and martensite clearly plays a more dominant role in strain partitioning. In a similar work, also coupling simulations to experiments, Woo et al. (185) focused on simple geometrical features to investigate the importance of ferrite crystallographic orientation. CP simulations to predict fracture were presented in References 92 and 180. The microstructure was analyzed and failure mechanisms experimentally derived as a function of strain. Void nucleation, growth, and coalescence were characterized. On the basis of the experimental observations and simulation results, a model describing the failure mechanism was thus proposed for DP steel. In these investigations, comparison to experiments was conducted only with respect to the global stress-strain response. Damage was found to originate essentially from the martensite. Chen et al. (186) described one of the most sophisticated approaches. Using micropillar tests, these researchers calibrated CP models for martensite and ferrite, taking non-Schmid effects on flow into account for ferrite and modeling the martensite as a hierarchical microstructure. The fitting parameters were then applied to realistic microstructures that were computer generated. The advantage of this approach is that 3D microstructures were probed and corresponding stress distributions on interfaces were predicted. The strain partitioning was hence used to explain the global stress-strain behavior. Significantly, the constitutive modeling of martensite in DP steels remains challenging because bulk martensite does not have the same carbon content and hierarchical microstructure as do the martensite islands in DP steels. The works by Ghassemi-Armaki et al. (85, 187) are related to the work of Chen et al. (186) but place more focus on modeling the constitutive response of

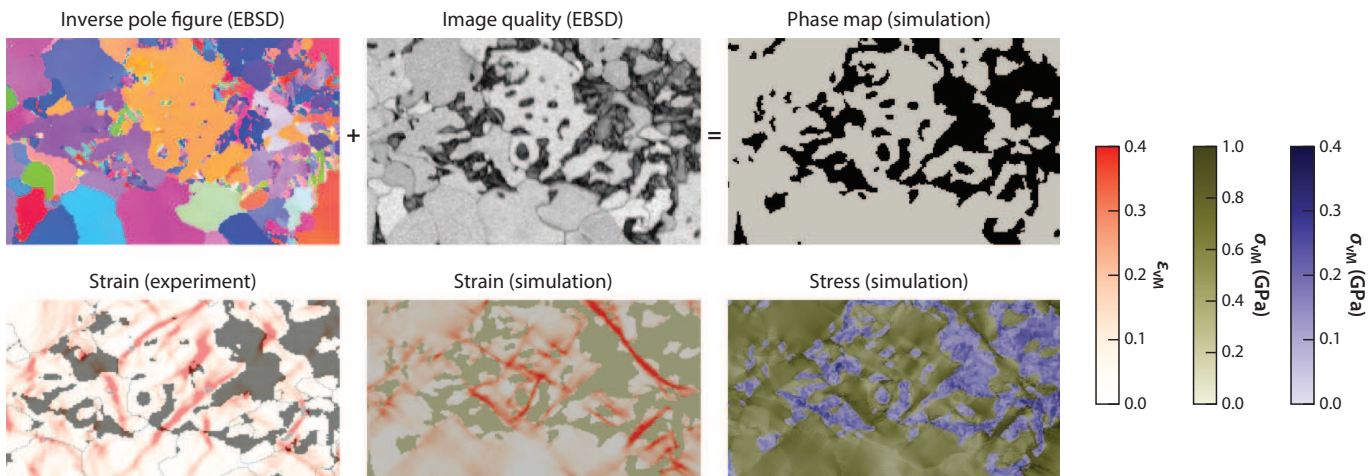


Figure 18

Integrated experiments and CP simulations enable simultaneous mapping of microstructure, microstrains, and microstresses. EBSD data (with image quality serving as the discriminator for the phase distribution) are used to create a CP model. The von Mises equivalent strain (ϵ_{vM}) distribution can be obtained from both simulation and experiment. The equivalent stress (σ_{vM}) distribution is accessible from CP simulations only. CP denotes crystal plasticity. Adapted from Reference 75 with permission.

the martensite phase. Tasan et al. (75) directly compared strain data obtained by μ DIC, enabling close coupling between simulation and experiments, as is shown in **Figure 18**.

Katani et al. (188) used a Gurson-Tvergaard-Needleman damage model in the ferrite and also considered the ferrite-martensite interfaces to show that the stress localization caused by the martensite provides the source for failure initiation. In contrast, Ramazani et al. (189) investigated the cracking in martensite by finite element modeling and found that the damage evolves in a spatially resolved manner. These results can be directly used for future alloy and process design strategies, as banded microstructures perform worse than their equiaxed counterparts. Similar work by Vajragupta et al. (190) included ductile damage in ferrite. In the work of Kim et al. (191), a microstructure patch is directly derived from a real microstructure and loaded according to the load path determined in an isotropic hole expansion simulation (see Section 4.2.1). A ductile failure criterion was used to predict failure at the microscale as well as the global failure evident in the stress-strain curve.

4.4. Challenges in the Simulation of the Mechanical Properties of DP Steels

The predictive capability of DP steel simulations has improved significantly in recent years, enabled by more accurate constitutive models, higher-fidelity morphology incorporation, and thorough coupling to experiments. Two remaining challenges to the quality of the models are the determination of individual phase and interface properties and the acquisition of realistic 3D microstructures.

Many experimental and theoretical efforts have been made, and analytical fitting methods have been used [e.g., by Tjahjanto et al. (192)] to obtain the mechanical properties of the two phases. Because it is hard to produce bulk single-phase ferrite and martensite specimens that resemble the constitutive state of the phases found in real DP microstructures, a common approach is to conduct selective small-scale testing directly on representative portions of the microstructure

under investigation. Tasan et al. (75) presented an approach based on nanoindentation. This approach is, however, limited to the determination of the ferrite properties. Chen et al. (186) presented modeling of micropillar compression tests by using a sophisticated CP model [more details on the experiments can be found in Ghassemi-Armaki (85)]. This approach is also applicable to martensitic pillars; however, because of the fine scale in martensite, the approach does not enable one to probe the behavior of a single-crystal orientation as is the case for ferrite in Reference 75.

Regarding the incorporation of realistic topological features, increasingly complex microstructures are being used for simulations, which in the future should be not only computationally generated but obtained from experiments. In this context, 3D EBSD and XRD microtomography are viable options. All the studies that are presented here and that rely on real microstructures use a surface-scanning technique to obtain experimental input data. However, as shown by Ramazani et al. (193), the response of a real 3D structure may differ from the response of 2D slices. Tasan et al. (75) discussed reasons for this difference. For building the simulations on representative microstructures, obtaining full 3D experimental data sets is therefore necessary. This is not only experimentally challenging but will also drastically increase the computational costs when structures large enough to correctly represent all features of a DP microstructure are used. The computer-aided generation of realistic RVEs, combining both geometric and metallurgical principles to simulate microstructures (194), is an important task to overcome experimental challenges. Related is the question of postprocessing experimental data to improve convergence and to omit artifacts in simulation results. Such improvements include methods for boundary smoothing (195).

5. CONCLUSIONS

Above we review the current status of research on microstructure-oriented processing in DP steels and the current understanding of the micromechanical processes involved during DP steel deformation. DP steels can be substantially affected by microstructure; chemical segregation; and process-dependent through-thickness gradients and inheritance effects of phase distribution, texture, and grain size. The relationship between microstructure and the mechanical performance of these materials is governed by several trends, such as the effects of V_M and C_M (both increase strength but reduce ductility) and the effects of decreasing ferrite grain size and increasing martensite dispersion (both lead to higher ductility and higher strength). Microstructural damage processes play a key role in these trends, and recent full-field simulations suggest that heterophase decohesion, martensite fracture, and sharp strain accumulation in percolating ferrite structures are relevant in this context.

In this regard, there are a number of research opportunities to better understand and ultimately improve DP steels. These possibilities include improving HE, chemical segregation effects, stress corrosion cracking, effects of welding and accumulative damage inherited from complex sheet-forming operations, and performance under dynamic loading. Improvement of the micromechanical behavior of DP steels and the introduction of novel microstructure design concepts require further insight into their microstructure and deformation substructures. New experimental and numerical techniques for characterizing and digitizing microstructures are briefly reviewed, underscoring the outstanding challenges and opportunities to improve the fidelity of methods used for capturing 3D microstructures. In situ and multiprobe experimental approaches and integrated experimental-simulation approaches are expected to remain important in unraveling the complexity of the interplay between the different phases in DP steels.

APPENDIX: ACRONYMS USED FOR EBSD AND TEXTURE ANALYSIS

Acronym	Definition
EBSQ IQ	Image quality: quality of an EBSD Kikuchi diffraction pattern
KAM	Kernel average misorientation: average misorientation between a point and all its neighbor points within a certain radius (here 400 nm) and excluding neighboring EBSD points with misorientations exceeding some tolerance value (here 3°)
GS	Grain orientation spread: average deviation between the orientation of each point in the grain and the average orientation for the grain
CI	Confidence index: unambiguity for indexing a diffraction pattern
FIT	Fit parameter: angular deviation between recalculated and detected Kikuchi bands
IPF/RD, IPF/ND	Inverse pole figure (IPF): position of the rolling direction (RD) and normal direction (ND) relative to the crystal reference frame
Orientation fiber	Description
α -Fiber	$\langle 110 \rangle \parallel RD; \varphi_1 = 0^\circ, \phi = 0\text{--}90^\circ, \varphi_2 = 45^\circ$; $\{001\}\langle\bar{1}\bar{0}\rangle, \{112\}\langle\bar{1}\bar{0}\rangle, \{111\}\langle\bar{1}\bar{0}\rangle$
γ -Fiber	$\{111\} \parallel ND; \varphi_1 = 0\text{--}90^\circ, \phi = 55^\circ, \varphi_2 = 45^\circ$; $\{111\}\langle\bar{1}\bar{0}\rangle, \{111\}\langle\bar{1}\bar{2}\rangle$
ε -Fiber	$\langle 110 \rangle \parallel TD; \varphi_1 = 90^\circ, \phi = 0\text{--}90^\circ, \varphi_2 = 45^\circ$; $\{001\}\langle\bar{1}0\rangle, \{4\bar{4}11\}\langle\bar{1}\bar{1}\bar{1}\bar{8}\rangle, \{112\}\langle\bar{1}\bar{1}1\rangle, \{111\}\langle\bar{1}\bar{1}2\rangle, \{11\bar{1}1\bar{8}\}\langle\bar{4}\bar{4}11\rangle, \{110\}\langle001\rangle$
η -Fiber	$\langle 100 \rangle \parallel RD; \varphi_1 = 0^\circ, \phi = 0\text{--}90^\circ, \varphi_2 = 0^\circ$; $\{001\}\langle100\rangle, \{011\}\langle100\rangle$
θ -Fiber	$\{001\} \parallel ND; \varphi_1 = 0\text{--}90^\circ, \phi = 0^\circ, \varphi_2 = 0^\circ$; $\{001\}\langle100\rangle, \{001\}\langle\bar{1}\bar{0}\rangle$
ζ -Fiber	$\{110\} \parallel ND; \varphi_1 = 0\text{--}90^\circ, \phi = 45^\circ, \varphi_2 = 0^\circ$; $\{011\}\langle100\rangle, \{011\}\langle2\bar{1}\bar{1}\rangle, \{011\}\langle\bar{1}\bar{1}1\rangle, \{011\}\langle0\bar{1}\bar{1}\rangle$
β -Skeleton line	$\{111\}$ close to ND; $\{111\}\langle\bar{1}\bar{0}\rangle, \{557\}\langle583\rangle, \{111\}\langle\bar{1}\bar{2}\rangle$

DISCLOSURE STATEMENT

The authors are not aware of any affiliations, memberships, funding, or financial holdings that might be perceived as affecting the objectivity of this review.

ACKNOWLEDGMENTS

Parts of this work were carried out under project number M 41.2.10410 in the framework of the research program of the material innovation institute M2i (<http://www.m2i.nl>). Funding from the European Research Council under the EU's seventh Framework Program (FP7/2007–2013)/ERC grant agreement 290998 is also gratefully acknowledged.

LITERATURE CITED

- Speich GR, Miller RL. 1979. Mechanical properties of ferrite-martensite steels. In *Structure and Properties of Dual-Phase Steels*, ed. RA Kot, JW Morris, pp. 145–82. New York: TMS-AIME
- Mazinani M, Poole WJ. 2007. Effect of martensite plasticity on the deformation behavior of a low-carbon dual-phase steel. *Metall. Mater. Trans. A* 38:328–39
- Korzekwa DA, Matlock DK, Krauss G. 1984. Dislocation substructure as a function of strain in a dual-phase steel. *Metall. Trans. A* 15(6):1221–28
- Ramos LF, Matlock DK, Krauss G. 1979. On the deformation behavior of dual-phase steels. *Metall. Trans. A* 10(2):259–61
- Davies RG. 1978. The mechanical properties of zero-carbon ferrite-plus-martensite structures. *Metall. Trans. A* 9(3):451–55

6. Zaeferer S, Elhami N-N. 2014. Theory and application of electron channelling contrast imaging under controlled diffraction conditions. *Acta Mater.* 75(154):20–50
7. Gutierrez-Urrutia I, Zaeferer S, Raabe D. 2013. Coupling of electron channeling with EBSD: toward the quantitative characterization of deformation structures in the SEM. *JOM* 65(9):1229–36
8. Calcagnotto M, Ponge D, Demir E, Raabe D. 2010. Orientation gradients and geometrically necessary dislocations in ultrafine grained dual-phase steels studied by 2D and 3D EBSD. *Mater. Sci. Eng. A* 527(10–11):2738–46
9. Schemman L. 2014. *The inheritance of different microstructures found after hot rolling on the properties of a completely annealed DP-steel*. PhD Thesis, RWTH Aachen Univ.
10. Zaeferer S. 2011. A critical review of orientation microscopy in SEM and TEM. *Cryst. Res. Technol.* 46(6):607–28
11. Benner G, Niebel H, Pavia G. 2011. Nano beam diffraction and precession in an energy filtered CS corrected transmission electron microscope. *Cryst. Res. Technol.* 46(6):580–88
12. Hirata A, Hirotsu Y, Matsubara E, Ohkubo T, Hono K. 2006. Mechanism of nanocrystalline microstructure formation in amorphous Fe-Bb-B alloys. *Phys. Rev. B* 74(18):184204
13. Zhang X, Godfrey A, Hansen N, Huang X. 2013. Hierarchical structures in cold-drawn pearlitic steel wire. *Acta Mater.* 61(13):4898–909
14. Mueller TO, Cowan J, Sanson E. 2007. The use of oxygen in SEM plasma cleaning equipment. *Microsc. Microanal.* 13(Suppl. 2):210–11
15. Pinard PT, Schwedt A. 2013. Characterization of dual-phase steel microstructure by combined submicrometer EBSD and EPMA carbon measurements. *Microsc. Microanal.* 19(4):996–1006
16. Lerchbacher C, Zinner S, Leitner H. 2012. Atom probe study of the carbon distribution in a hardened martensitic hot-work tool steel X38CrMoV5-1. *Micron* 43(7):818–26
17. Dmitrieva O, Ponge D, Inden G, Millán J, Choi P, et al. 2011. Chemical gradients across phase boundaries between martensite and austenite in steel studied by atom probe tomography and simulation. *Acta Mater.* 59(1):364–74
18. Hutchinson B, Hagström J, Karlsson O. 2011. Microstructures and hardness of as-quenched martensites (0.1–0.5% C). *Acta Mater.* 59(14):5845–58
19. Herbig M, Raabe D, Li YJ, Choi P, Zaeferer S, Goto S. 2014. Atomic-scale quantification of grain boundary segregation in nanocrystalline material. *Phys. Rev. Lett.* 112(12):126103
20. Marceau RKW, Gutierrez-Urrutia I, Herbig M, Moore KL, Lozano-Perez S, Raabe D. 2013. Multi-scale correlative microscopy investigation of both structure and chemistry of deformation twin bundles in Fe-Mn-C steel. *Microsc. Microanal.* 19(6):1581–85
21. Ray RK. 1984. Texture in an intercritically annealed dual-phase steel. *Scr. Metall.* 18:1211–14
22. Ray RK. 1986. Orientation distribution function analysis of texture in a dual-phase steel. *Mater. Sci. Eng.* 77:169–74
23. Mondal DK, Ray RK. 1992. Development of {111} texture during cold rolling and recrystallization of a C-Mn-V dual-phase steel. *Mater. Sci. Eng. A* 158(2):147–56
24. Chowdhury SG, Pereloma EV, Santos DB. 2008. Evolution of texture at the initial stages of continuous annealing of cold rolled dual-phase steel: effect of heating rate. *Mater. Sci. Eng. A* 480(1–2):540–48
25. Garday B, Bouvier S, Richard V, Bacoux B. 2005. Texture and dislocation structures observation in a dual-phase steel under strain-path changes at large deformation. *Mater. Sci. Eng. A* 400–401:136–41
26. Rocha RO, Melo TMF, Pereloma EV, Santos DB. 2005. Microstructural evolution at the initial stages of continuous annealing of cold rolled dual-phase steel. *Mater. Sci. Eng. A* 391(1–2):296–304
27. Calcagnotto M, Ponge D, Raabe D. 2008. Ultrafine grained ferrite/martensite dual phase steel fabricated by large strain warm deformation and subsequent intercritical annealing. *ISIJ Int.* 48(8):1096–101
28. Zheng YS, Wang ZG, Ai SH. 1994. Effect of dislocation substructure of crack tip on near fatigue threshold in dual-phase steels. *Mater. Sci. Eng. A* 176(1–2):393–96
29. Qu J, Dabboussi W, Hassani F, Nemes J, Yue S. 2008. Effect of microstructure on the dynamic deformation behavior of dual phase steel. *Mater. Sci. Eng. A* 479(1–2):93–104
30. Hölscher M, Raabe D, Lücke K. 1994. Relationship between rolling textures and shear textures in fcc and bcc metals. *Acta Metall. Mater.* 42(3):879–86

31. Raabe D. 2003. Overview on basic types of hot rolling textures of steels. *Steel Res. Int.* 74(5):327–37
32. Landau LD. 1937. Theory of phase transformations. *Zh. Eksp. Teor. Fiz.* 7:19–32
33. Huh M, Lee J, Park SH, Engler O, Raabe D. 2005. Effect of through-thickness macro and micro-texture gradients on ridging of 17% Cr ferritic stainless steel sheet. *Steel Res. Int.* 76(11):797–806
34. Raabe D, Lücke K. 1993. Textures of ferritic stainless steels. *Mater. Sci. Technol.* 9:302–12
35. Speich GR, Demarest VA, Miller RL. 1981. Formation of austenite during intercritical annealing of dual-phase steels. *Metall. Mater. Trans. A* 12(8):1419–28
36. Kim S, Lee S. 2000. Effects of martensite morphology and volume fraction on quasi-static and dynamic deformation behavior of dual-phase steels. *Metall. Mater. Trans. A* 31(7):1753–60
37. Jiang Z, Guan Z, Lian J, Mechanics F. 1995. Effects of microstructural variables on the deformation behaviour of dual-phase steel. *Mater. Sci. Eng. A* 190(1–2):55–64
38. Nakajima K, Urabe T, Hosoya Y, Kamishi S, Miyata T, Takeda N. 2001. Influence of microstructural morphology and prestraining on short fatigue crack propagation in dual-phase steels. *ISIJ Int.* 41(3):298–304
39. Matlock DK, Zia-Ebrahimi F, Krauss G. 1982. Structure, properties and strain hardening of dual-phase steels. In *Deform. Process. Struct.*, pp. 47–87
40. Peranio N, Li YJ, Roters F, Raabe D. 2010. Microstructure and texture evolution in dual-phase steels: competition between recovery, recrystallization, and phase transformation. *Mater. Sci. Eng. A* 527(16–17):4161–68
41. Peranio N, Roters F, Raabe D. 2012. Microstructure evolution during recrystallization in dual-phase steels. *Mater. Sci. Forum* 715–716:13–22
42. Yang DZ, Brown EL, Matlock DK, Krauss G. 1985. Ferrite recrystallization and austenite formation in cold-rolled intercritically annealed steel. *Metall. Trans. A* 16(8):1385–92
43. Huang J, Poole WJ, Militzer M. 2004. Austenite formation during intercritical annealing. *Metall. Mater. Trans. A* 35(11):3363–75
44. Azizi-Alizamini H, Militzer M, Poole WJ. 2010. Austenite formation in plain low-carbon steels. *Metall. Mater. Trans. A* 42(6):1544–57
45. Militzer M. 2011. Phase field modeling of microstructure evolution in steels. *Curr. Opin. Solid State Mater. Sci.* 15(3):106–15
46. Rudnizki J, Böttger B, Prah U, Bleck W. 2011. Phase-field modeling of austenite formation from a ferrite plus pearlite microstructure during annealing of cold-rolled dual-phase steel. *Metall. Mater. Trans. A* 42(8):2516–25
47. Bos C, Mecozzi MG, Sietsma J. 2010. A microstructure model for recrystallisation and phase transformation during the dual-phase steel annealing cycle. *Comput. Mater. Sci.* 48(3):692–99
48. Bos C, Mecozzi MG, Hanlon DN, Aarnts MP, Sietsma J. 2011. Application of a three-dimensional microstructure evolution model to identify key process settings for the production of dual-phase steels. *Metall. Mater. Trans. A* 42(12):3602–10
49. Okuda K, Yoshida H, Nagataki Y, Tanaka Y, Rollett AD. 2007. Preliminary simulation for competing behaviors between recrystallization and transformation in dual phase steels. *Mater. Sci. Forum* 558–559:1145–50
50. Savran VI, Van Leeuwen Y, Hanlon DN, Kwakernaak C, Sloof WG, Sietsma J. 2007. Microstructural features of austenite formation in C35 and C45 alloys. *Metall. Mater. Trans. A* 38(5):946–55
51. Savran VI, Offerman SE, Sietsma J. 2010. Austenite nucleation and growth observed on the level of individual grains by three-dimensional X-ray diffraction microscopy. *Metall. Mater. Trans. A* 41(3):583–91
52. Krielaart GP, Sietsma J, van der Zwaag S. 1997. Ferrite formation in Fe-C alloys during austenite decomposition under non-equilibrium interface conditions. *Mater. Sci. Eng. A* 237:216–23
53. Loginova I, Odqvist J, Amberg G, Ågren J. 2003. The phase-field approach and solute drag modeling of the transition to massive $\gamma \rightarrow \alpha$ transformation in binary Fe-C alloys. *Acta Mater.* 51(5):1327–39
54. Zheng C, Raabe D. 2013. Interaction between recrystallization and phase transformation during intercritical annealing in a cold-rolled dual-phase steel: a cellular automaton model. *Acta Mater.* 61(14):5504–17

55. Zheng C, Raabe D, Li D. 2012. Prediction of post-dynamic austenite-to-ferrite transformation and reverse transformation in a low-carbon steel by cellular automaton modeling. *Acta Mater.* 60(12):4768–79
56. Masimov M, Peranio N, Springub B, Roters F, Raabe D. 2010. EBSD study of substructure and texture formation in dual-phase steel sheets for semi-finished products. *Solid State Phenom.* 160:251–56
57. Fedosseev AI, Raabe D. 1994. Application of the method of superposition of harmonic currents for the simulation of inhomogeneous deformation during hot rolling of FeCr. *Scr. Metall. Mater.* 30(1):1–6
58. Aborn RH. 1956. Low carbon martensite. *Trans. ASM* 48:51–85
59. Waterschoot T, Verbeken K, De Cooman BC. 2006. Tempering kinetics of the martensitic phase in DP steel. *ISIJ Int.* 46(1):138–46
60. Krauss G. 1995. Heat treated martensitic steels: microstructural systems for advanced manufacture. *ISIJ Int.* 35(4):349–59
61. Calcagnotto M, Adachi Y, Ponge D, Raabe D. 2011. Deformation and fracture mechanisms in fine- and ultrafine-grained ferrite/martensite dual-phase steels and the effect of aging. *Acta Mater.* 59(2):658–70
62. Kim S-J, Cho Y-G, Oh C-S, Kim DE, Moon MB, Han HN. 2009. Development of a dual phase steel using orthogonal design method. *Mater. Des.* 30(4):1251–57
63. Raabe D. 2007. Multiscale recrystallization models for the prediction of crystallographic textures with respect to process simulation. *J. Strain Anal. Eng. Des.* 42(4):253–68
64. Zhu B, Militzer M. 2015. Phase-field modeling for intercritical annealing of a dual-phase steel. *Metall. Mater. Trans. A* 46(3):1073–84
65. Offerman SE, van Dijk NH, Sietsma J, Lauridsen EM, Margulies L, et al. 2004. Solid-state phase transformations involving solute partitioning: modeling and measuring on the level of individual grains. *Acta Mater.* 52(16):4757–66
66. Bos C, Sietsma J. 2007. A mixed-mode model for partitioning phase transformations. *Scr. Mater.* 57(12):1085–88
67. Song X, Rettenmayr M, Müller C, Exner HE. 2001. Modeling of recrystallization after inhomogeneous deformation. *Metall. Mater. Trans. A* 32(9):2199–206
68. Raabe D, Hantcherli L. 2005. 2D cellular automaton simulation of the recrystallization texture of an IF sheet steel under consideration of Zener pinning. *Comput. Mater. Sci.* 34(4):299–313
69. Raabe D. 1999. Introduction of a scalable three-dimensional cellular automaton with a probabilistic switching rule for the discrete mesoscale simulation of recrystallization phenomena. *Philos. Mag. A* 79(10):2339–58
70. Roters F, Eisenlohr P, Hantcherli L, Tjahjanto DD, Bieler TR, Raabe D. 2010. Overview of constitutive laws, kinematics, homogenization and multiscale methods in crystal plasticity finite-element modeling: theory, experiments, applications. *Acta Mater.* 58(4):1152–211
71. Rashid MS. 1981. Dual phase steels. *Annu. Rev. Mater. Sci.* 11:245–66
72. Dutta VB, Suresh S, Ritchie RO. 1984. Fatigue crack propagation in dual-phase steels: effects of ferritic-martensitic microstructures on crack path morphology. *Metall. Trans. A* 15:1193–207
73. Huh H, Kim SB, Song JH, Lim JH. 2008. Dynamic tensile characteristics of TRIP-type and DP-type steel sheets for an auto-body. *Int. J. Mech. Sci.* 50:918–31
74. Grässel O, Krüger L, Frommeyer G, Meyer LW. 2000. High strength Fe-Mn-(Al, Si) TRIP/TWIP steels development-properties-application. *Int. J. Plast.* 16:1391–409
75. Tasan CC, Diehl M, Yan D, Zambaldi C, Shanthraj P, et al. 2014. Integrated experimental-simulation analysis of stress and strain partitioning in multiphase alloys. *Acta Mater.* 81:386–400
76. Shen HP, Lei TC, Liu JZ. 1986. Microscopic deformation behaviour of martensitic-ferritic dual-phase steels. *Mater. Sci. Technol.* 2(1):28–33
77. Kang J, Ososkov Y, Embury JD, Wilkinson DS. 2007. Digital image correlation studies for microscopic strain distribution and damage in dual phase steels. *Scr. Mater.* 56(11):999–1002
78. Tasan CC, Hoefnagels JPM, Geers MGD. 2010. Microstructural banding effects clarified through micrographic digital image correlation. *Scr. Mater.* 62(11):835–38
79. Ghadbeigi H, Pinna C, Celotto S, Yates JR. 2010. Local plastic strain evolution in a high strength dual-phase steel. *Mater. Sci. Eng. A* 527(18–19):5026–32

80. Kapp M, Hebesberger T, Kolednik O. 2011. A micro-level strain analysis of a high-strength dual-phase steel. *Int. J. Mater. Res.* 102(6):687–91
81. Joo S-H, Lee JK, Koo J-M, Lee S, Suh D-W, Kim HS. 2013. Method for measuring nanoscale local strain in a dual phase steel using digital image correlation with nanodot patterns. *Scr. Mater.* 68(5):245–48
82. Marteau J, Haddadi H, Bouvier S. 2012. Investigation of strain heterogeneities between grains in ferritic and ferritic-martensitic steels. *Exp. Mech.* 53(3):427–39
83. Han Q, Kang Y, Hodgson PD, Stanford N. 2013. Quantitative measurement of strain partitioning and slip systems in a dual-phase steel. *Scr. Mater.* 69(1):13–16
84. Tasan CC, Hoefnagels JPM, Diehl M, Yan D, Roters F, Raabe D. 2014. Strain localization and damage in dual phase steels investigated by coupled in-situ deformation experiments and crystal plasticity simulations. *Int. J. Plast.* 63:198–210
85. Ghassemi-Armaki H, Maaß R, Bhat SP, Sriram S, Greer JR, Kumar KS. 2014. Deformation response of ferrite and martensite in a dual-phase steel. *Acta Mater.* 62:197–211
86. Maire E, Bouaziz O, Di Michiel M, Verdu C. 2008. Initiation and growth of damage in a dual-phase steel observed by X-ray microtomography. *Acta Mater.* 56(18):4954–64
87. Stevenson R. 1979. Crack initiation and propagation in thermal mechanically treated sheet steels. In *Formable HSLA and Dual Phase Steels*, ed. AT Davenport, pp. 99–108. New York: TMS-AIME
88. Avramovic-Cingara G, Saleh CAR, Jain MK, Wilkinson DS. 2009. Void nucleation and growth in dual-phase steel 600 during uniaxial tensile testing. *Metall. Mater. Trans. A* 40(13):3117–27
89. Avramovic-Cingara G, Ososkov Y, Jain MK, Wilkinson DS. 2009. Effect of martensite distribution on damage behaviour in DP600 dual phase steels. *Mater. Sci. Eng. A* 516(1–2):7–16
90. He XJ, Terao N, Berghezan A. 1984. Influence of martensite morphology and its dispersion on mechanical properties and fracture mechanisms of Fe-Mn-C dual phase steels. *Met. Sci.* 18:367–73
91. Azuma M, Goutianos S, Hansen N, Winther G, Huang X. 2012. Effect of hardness of martensite and ferrite on void formation in dual phase steel. *Mater. Sci. Technol.* 28(9–10):1092–100
92. Kadkhodapour J, Butz A, Ziae Rad S. 2011. Mechanisms of void formation during tensile testing in a commercial, dual-phase steel. *Acta Mater.* 59(7):2575–88
93. Tasan CC, Hoefnagels JPM, ten Horn CHLJ, Geers MGD. 2009. Experimental analysis of strain path dependent ductile damage mechanics and forming limits. *Mech. Mater.* 41(11):1264–76
94. Lee HS, Hwang B, Lee S, Lee CG, Kim SJ. 2004. Effects of martensite morphology and tempering on dynamic deformation behavior of dual-phase steels. *Metall. Mater. Trans. A* 35(8):2371–82
95. Erdogan M. 2002. The effect of new ferrite content on the tensile fracture behaviour of dual phase steels. *J. Mater. Process. Technol.* 37(7):3623–30
96. Kang S-M, Kwon H. 1987. Fracture behavior of intercritically treated complex structure in medium-carbon 6Ni steel. *Metall. Trans. A* 18(9):1587–92
97. Sun S, Pugh M. 2002. Properties of thermomechanically processed dual-phase steels containing fibrous martensite. *Mater. Sci. Eng. A* 335(1–2):298–308
98. Kim NJ, Thomas G. 1981. Effects of morphology on the mechanical behavior of a dual phase Fe/2Si/0.1C steel. *Metall. Trans. A* 12(3):483–89
99. Sarwar M, Priestner R. 1996. Influence of ferrite-martensite microstructural morphology on tensile properties of dual-phase steel. *J. Mater. Sci.* 31:2091–95
100. Steinbrunner DL, Matlock DK, Krauss G. 1988. Void formation during tensile testing of dual phase steels. *Metall. Trans. A* 19(3):579–89
101. Koyama M, Tasan CC, Akiyama E, Tsuzaki K, Raabe D. 2014. Hydrogen-assisted decohesion and localized plasticity in dual-phase steel. *Acta Mater.* 70:174–87
102. Davies RG. 1981. Hydrogen embrittlement of dual-phase steels. *Metall. Trans. A* 12(9):1667–72
103. Davies RG. 1983. Influence of martensite content on the hydrogen embrittlement of dual-phase steels. *Scr. Metall.* 17(7):889–92
104. Toji Y, Takagi S, Yoshino M, Hasegawa K, Tanaka Y. 2010. Evaluation of hydrogen embrittlement for high strength steel sheets. *Mater. Sci. Forum* 638–642:3537–42
105. Marder AR. 1982. Deformation characteristics of dual-phase steels. *Metall. Trans. A* 13:85–92
106. Ahmad E, Manzoor T, Ali KL, Akhter JI. 2000. Effect of microvoid formation on the tensile properties of dual-phase steel. *J. Mater. Eng. Perform.* 9(6):306–10

107. Azizi-Alizamini H, Militzer M, Poole WJ. 2011. Formation of ultrafine grained dual phase steels through rapid heating. *ISIJ Int.* 51(6):958–64
108. Bergström Y, Granbom Y, Sterkenburg D. 2010. A dislocation-based theory for the deformation hardening behavior of DP steels: impact of martensite content and ferrite grain size. *J. Metall.* 2010:1–16
109. Davies RG. 1978. Influence of martensite composition and content on the properties of dual phase steels. *Metall. Trans. A* 9:671–79
110. Nakada N, Arakawa Y, Park K-S, Tsuchiyama T, Takaki S. 2012. Dual phase structure formed by partial reversion of cold-deformed martensite. *Mater. Sci. Eng. A* 553:128–33
111. Park K-T, Lee YK, Shin DH. 2005. Fabrication of ultrafine grained ferrite/martensite dual phase steel by severe plastic deformation. *ISIJ Int.* 45(5):750–55
112. Shin DH, Kim WG, Ahn JY, Park K. 2006. Ultrafine grained dual phase steels fabricated by equal channel angular pressing. *Mater. Sci. Forum* 504:447–53
113. Zhang MD, Hu J, Cao WQ, Dong H. 2014. Microstructure and mechanical properties of high strength and high toughness micro-laminated dual phase steels. *Mater. Sci. Eng. A* 618:168–75
114. Szewczyk AF, Gurland J. 1982. A study of the deformation and fracture of a dual-phase steel. *Metall. Trans. A* 13(10):1821–26
115. Zhang H, Ponge D, Raabe D. 2014. Designing quadplex (four-phase) microstructures in an ultrahigh carbon steel. *Mater. Sci. Eng. A* 612:46–53
116. Pierman A-P, Bouaziz O, Pardoén T, Jacques PJ, Brassart L. 2014. The influence of microstructure and composition on the plastic behaviour of dual-phase steels. *Acta Mater.* 73:298–311
117. Maresca F, Kouznetsova V, Geers MGD. 2014. On the role of interlath retained austenite in the deformation of lath martensite. *Model. Simul. Mater. Sci. Eng.* 22(4):045011
118. Maresca F, Kouznetsova V, Geers MGD. 2014. Subgrain lath martensite mechanics: a numerical-experimental analysis. *J. Mech. Phys. Solids* 73:69–83
119. Yuan L, Ponge D, Wittig J, Choi P, Jiménez JA, Raabe D. 2012. Nanoscale austenite reversion through partitioning, segregation and kinetic freezing: example of a ductile 2 GPa Fe-Cr-C steel. *Acta Mater.* 60:2790–804
120. Papa Rao M, Subramanya Sarma V, Sankaran S. 2014. Processing of bimodal grain-sized ultrafine-grained dual phase microalloyed V-Nb steel with 1370 MPa strength and 16 pct uniform elongation through warm rolling and intercritical annealing. *Metall. Mater. Trans. A* 45(12):5313–17
121. Lai Q, Bouaziz O, Bréchet Y, Gouné M, Pardoén T. 2013. *Phase transformation controlled architectures in steel alloys*. Presented at EUROMAT 2013, Sept. 8–13, Sevilla, Spain
122. Chang P-H, Preban AG. 1985. The effect of ferrite grain-size and martensite volume fraction on the tensile properties of dual phase steel. *Acta Metall. Mater.* 33(5):897–903
123. Son YI, Lee YK, Park K-T, Lee CS, Shin DH. 2005. Ultrafine grained ferrite–martensite dual phase steels fabricated via equal channel angular pressing: microstructure and tensile properties. *Acta Mater.* 53(11):3125–34
124. Tsipouridis P, Werner E, Krempaszky C, Tragl E. 2006. Formability of high strength dual-phase steels. *Steel Res. Int.* 77(9–10):654–67
125. Delincé M, Bréchet Y, Embury JD, Geers MGD, Jacques PJ, Pardoén T. 2007. Structure–property optimization of ultrafine-grained dual-phase steels using a microstructure-based strain hardening model. *Acta Mater.* 55(7):2337–50
126. Mukherjee K, Hazra SS, Militzer M. 2009. Grain refinement in dual-phase steels. *Metall. Mater. Trans. A* 40(9):2145–59
127. Calcagnotto M, Ponge D, Raabe D. 2011. On the effect of manganese on grain size stability and hardenability in ultrafine-grained ferrite/martensite dual-phase steels. *Metall. Mater. Trans. A* 43(1):37–46
128. Calcagnotto M, Ponge D, Raabe D. 2012. Microstructure control during fabrication of ultrafine grained dual-phase steel: characterization and effect of intercritical annealing parameters. *ISIJ Int.* 52(5):874–83
129. Calcagnotto M, Ponge D, Raabe D. 2010. Effect of grain refinement to 1 μm on strength and toughness of dual-phase steels. *Mater. Sci. Eng. A* 527(29–30):7832–40
130. Tsuji N. 2010. New routes for fabricating ultrafine-grained microstructures in bulky steels without very-high strains. *Adv. Eng. Mater.* 12(8):701–7

131. Karlsson B, Sundström BO. 1974. Inhomogeneity in plastic deformation of two-phase steels. *Mater. Sci. Eng.* 16(1–2):161–68
132. Helm D, Butz A, Raabe D, Gumbsch P. 2011. Microstructure-based description of the deformation of metals: theory and application. *JOM* 63(Apr.):26–33
133. Raabe D, Klose P, Engl B, Imlau KP, Friedel F, Roters F. 2002. Concepts for integrating plastic anisotropy into metal forming simulations. *Adv. Eng. Mater.* 4(4):169–80
134. Huh J, Huh H, Lee CS. 2013. Effect of strain rate on plastic anisotropy of advanced high strength steel sheets. *Int. J. Plast.* 44:23–46
135. Wang W-R, He C-W, Zhao Z-H, Wei X-C. 2011. The limit drawing ratio and formability prediction of advanced high strength dual-phase steels. *Mater. Des.* 32(6):3320–27
136. Lim H, Lee MG, Sung JH, Kim JH, Wagoner RH. 2012. Time-dependent springback of advanced high strength steels. *Int. J. Plast.* 29:42–59
137. Tarigopula V, Hopperstad OS, Langseth M. 2008. A study of localisation in dual-phase high-strength steels under dynamic loading using digital image correlation and FE analysis. *Int. J. Solids Struct.* 45(2):601–19
138. Qin J, Chen R, Wen X, Lin Y, Liang M, Lu F. 2013. Mechanical behaviour of dual-phase high-strength steel under high strain rate tensile loading. *Mater. Sci. Eng. A* 586:62–70
139. Banu M, Takamura M, Hama T, Naidim O, Teodosiu C, Makinouchi A. 2006. Simulation of springback and wrinkling in stamping of a dual phase steel rail-shaped part. *J. Mater. Process. Technol.* 173(2):178–84
140. Chen P, Koç M. 2007. Simulation of springback variation in forming of advanced high strength steels. *J. Mater. Process. Technol.* 190(1–3):189–98
141. Firat M. 2012. A finite element modeling and prediction of stamping formability of a dual-phase steel in cup drawing. *Mater. Des.* 34:32–39
142. Tarigopula V, Hopperstad OS, Langseth M. 2008. Elastic-plastic behaviour of dual-phase, high-strength steel under strain-path changes. *Eur. J. Mech. A* 27(5):764–82
143. Galantucci LM, Tricarico L. 1999. Thermo-mechanical simulation of a rolling process with an FEM approach. *J. Mater. Process. Technol.* 92–93:494–501
144. Gruben G, Hopperstad OS, Børvik T. 2012. Simulation of ductile crack propagation in dual-phase steel. *Int. J. Fract.* 180(1):1–22
145. Tarigopula V, Hopperstad OS, Langseth M, Clausen AH, Hild F, et al. 2008. A study of large plastic deformations in dual phase steel using digital image correlation and FE analysis. *Exp. Mech.* 48(2):181–96
146. Kim JH, Sung JH, Piao K, Wagoner RH. 2011. The shear fracture of dual-phase steel. *Int. J. Plast.* 27(10):1658–76
147. Luo M, Wierzbicki T. 2010. Numerical failure analysis of a stretch-bending test on dual-phase steel sheets using a phenomenological fracture model. *Int. J. Solids Struct.* 47(22–23):3084–102
148. Lian J, Vajragupta N, Münstermann S, Bleck W. 2011. On application of a damage plasticity model to sheet metal forming of DP steel. *Steel Res. Int.* (Spec. Ed. 10th Int. Conf. Technol. Plast.), pp. 901–6
149. Hu ZG, Zhu P, Meng J. 2010. Fatigue properties of transformation-induced plasticity and dual-phase steels for auto-body lightweight: experiment, modeling and application. *Mater. Des.* 31(6):2884–90
150. Tjahjanto DD, Eisenlohr P, Roters F. 2010. A novel grain cluster-based homogenization scheme. *Model. Simul. Mater. Sci. Eng.* 18(1):015006
151. Roters F, Eisenlohr P, Kords C, Tjahjanto DD, Diehl M, Raabe D. 2012. Damask: the Düsseldorf Advanced MAterial Simulation Kit for studying crystal plasticity using an FE based or a spectral numerical solver. *Proc. IUTAM* 3:3–10
152. Schröder J, Balzani D, Brands D. 2011. Approximation of random microstructures by periodic statistically similar representative volume elements based on lineal-path functions. *Arch. Appl. Mech.* 81(7):975–97
153. Uthaisangsuk V, Prahl U, Bleck W. 2009. Stretch-flangeability characterisation of multiphase steel using a microstructure based failure modelling. *Comput. Mater. Sci.* 45(3):617–23
154. Prawoto Y, Fanone M, Shahidi S, Ismail MS, Wan Nik WB. 2012. Computational approach using Johnson–Cook model on dual phase steel. *Comput. Mater. Sci.* 54:48–55
155. Al-Abbasi FM, Nemes JA. 2003. Micromechanical modeling of dual phase steels. *Int. J. Mech. Sci.* 45(9):1449–65

156. Mileiko ST. 1969. The tensile strength and ductility of continuous fibre composites. *J. Mater. Sci.* 4:974–77
157. Korzekwa DA, Lawson RD, Matlock DK, Krauss G. 1980. A consideration of models describing the strength and ductility of dual-phase steels. *Scr. Metall.* 14(9):1023–28
158. Mori T, Tanaka K. 1973. Average stress in matrix and average elastic energy of materials with misfitting inclusions. *Acta Metall.* 21(5):571–74
159. Tomota Y, Tamura I. 1982. Mechanical behavior of steels consisting of two ductile phases. *Trans. Iron Steel Inst. Jpn.* 22(9):665–77
160. Tomota Y, Kuroki K, Mori T, Tamura I. 1976. Tensile deformation of two-ductile-phase alloys: flow curves of α - γ Fe-Cr-Ni alloys. *Mater. Sci. Eng.* 24(1):85–94
161. Gurland J. 1979. A structural approach to the yield strength of two-phase alloys with coarse microstructures. *Mater. Sci. Eng.* 40(1):59–71
162. Bhadeshia HKDH, Edmonds DV. 1980. Analysis of mechanical properties and microstructure of high-silicon dual-phase steel. *Met. Sci.* 14(3):41–49
163. Goel NC, Sangal S, Tangri K. 1985. A theoretical model for the flow behavior of commercial dual-phase steels containing metastable retained austenite. Part I. Derivation of flow curve equations. *Metall. Trans. A* 16(11):2013–21
164. Paruz H, Edmonds DV. 1989. The strain hardening behaviour of dual-phase steel. *Mater. Sci. Eng. A* 17:67–74
165. Lian J, Jiang Z, Liu J. 1991. Theoretical model for the tensile work hardening behaviour of dual-phase steel. *Mater. Sci. Eng. A* 147(1):55–65
166. Bouaziz O, Lung T, Kandel M, Lecomte C. 2001. Physical modelling of microstructure and mechanical properties of dual-phase steel. *J. Phys. IV Fr.* 11(4):Pr4-223–31
167. Yoshida K, Brenner R, Bacroix B, Bouvier S. 2011. Micromechanical modeling of the work-hardening behavior of single- and dual-phase steels under two-stage loading paths. *Mater. Sci. Eng. A* 528(3):1037–46
168. Tsuchida N, Izaki Y, Tanaka T, Fukaura K. 2012. Effects of temperature and strain rate on stress-strain curves for dual-phase steels and their calculations by using the Kocks-Mecking model. *ISIJ Int.* 52(4):729–34
169. Thomser C, Uthaisangsuk V, Bleck W. 2009. Influence of martensite distribution on the mechanical properties of dual phase steels: experiments and simulation. *Steel Res. Int.* 80(8):582–87
170. Marvi-Mashhad M, Mazinani M, Rezaee-Bazzaz A. 2012. FEM modeling of the flow curves and failure modes of dual phase steels with different martensite volume fractions using actual microstructure as the representative volume. *Comput. Mater. Sci.* 65:197–202
171. Dong H-F, Li J, Zhang Y, Park J, Yang Q-X. 2010. Numerical simulation on the microstress and microstrain of low Si-Mn-Nb dual-phase steel. *Int. J. Miner. Metall. Mater.* 17(2):173–78
172. Ramazani A, Mukherjee K, Prahl U, Bleck W. 2012. Transformation-induced, geometrically necessary, dislocation-based flow curve modeling of dual-phase steels: effect of grain size. *Metall. Mater. Trans. A* 43(10):3850–69
173. Brands D, Schröder J, Balzani D, Dmitrieva O, Raabe D. 2011. On the reconstruction and computation of dual-phase steel microstructures based on 3D EBSD data. *PAMM* 11(1):503–4
174. Liedl U, Traint S, Werner E. 2002. An unexpected feature of the stress-strain diagram of dual-phase steel. *Comput. Mater. Sci.* 25(1–2):122–28
175. Asgari SA, Hodgson PD, Yang C, Rolfe BF. 2009. Modeling of advanced high strength steels with the realistic microstructure-strength relationships. *Comput. Mater. Sci.* 45(4):860–66
176. Tvergaard V. 1982. On localization in ductile materials containing spherical voids. *Int. J. Fract.* 18(4):237–52
177. Delannay L, Doghri I, Pierard O. 2007. Prediction of tension-compression cycles in multiphase steel using a modified incremental mean-field model. *Int. J. Solids Struct.* 44(22–23):7291–306
178. Paul SK, Kumar A. 2012. Micromechanics based modeling to predict flow behavior and plastic strain localization of dual phase steels. *Comput. Mater. Sci.* 63:66–74
179. Paul SK. 2013. Real microstructure based micromechanical model to simulate microstructural level deformation behavior and failure initiation in DP 590 steel. *Mater. Des.* 44:397–406

180. Kadkhodapour J, Butz A, Ziae-Rad S, Schmauder S. 2011. A micro mechanical study on failure initiation of dual phase steels under tension using single crystal plasticity model. *Int. J. Plast.* 27(7):1103–25
181. Sun X, Choi KS, Soulami A, Liu WN, Khaleel MA. 2009. On key factors influencing ductile fractures of dual phase (DP) steels. *Mater. Sci. Eng. A* 526(1–2):140–49
182. Sodjit S, Uthaisangsuk V. 2012. Microstructure based prediction of strain hardening behavior of dual phase steels. *Mater. Des.* 41:370–79
183. Kadkhodapour J, Schmauder S, Raabe D, Ziae-Rad S, Weber U, Calcagnotto M. 2011. Experimental and numerical study on geometrically necessary dislocations and non-homogeneous mechanical properties of the ferrite phase in dual phase steels. *Acta Mater.* 59(11):4387–94
184. Choi S-H, Kim E-Y, Woo W, Han SH, Kwak JH. 2013. The effect of crystallographic orientation on the micromechanical deformation and failure behaviors of DP980 steel during uniaxial tension. *Int. J. Plast.* 45:85–102
185. Woo W, Em VT, Kim E-Y, Han SH, Han YS, Choi S-H. 2012. Stress-strain relationship between ferrite and martensite in a dual-phase steel studied by in situ neutron diffraction and crystal plasticity theories. *Acta Mater.* 60(20):6972–81
186. Chen P, Ghassemi-Armaki H, Kumar S, Bower A, Bhat S, Sadagopan S. 2014. Microscale-calibrated modeling of the deformation response of dual-phase steels. *Acta Mater.* 65:133–49
187. Ghassemi-Armaki H, Chen P, Bhat S, Sadagopan S, Kumar S, Bower A. 2013. Microscale-calibrated modeling of the deformation response of low-carbon martensite. *Acta Mater.* 61(10):3640–52
188. Katani S, Ziae-Rad S, Nouri N, Saeidi N, Kadkhodapour J, et al. 2013. Microstructure modelling of dual-phase steel using SEM micrographs and Voronoi polycrystal models. *Metallogr. Microstruct. Anal.* 2(3):156–69
189. Ramazani A, Ebrahimi Z, Prahl U. 2014. Study the effect of martensite banding on the failure initiation in dual-phase steel. *Comput. Mater. Sci.* 87:241–47
190. Vajragupta N, Uthaisangsuk V, Schmaling B, Münstermann S, Hartmaier A, Bleck W. 2012. A micromechanical damage simulation of dual phase steels using XFEM. *Comput. Mater. Sci.* 54:271–79
191. Kim JH, Lee MG, Kim D, Matlock DK, Wagoner RH. 2010. Hole-expansion formability of dual-phase steels using representative volume element approach with boundary-smoothing technique. *Mater. Sci. Eng. A* 527(27–28):7353–63
192. Tjahjanto DD, Turteltaub S, Suiker ASJ, van der Zwaag S. 2006. Modelling of the effects of grain orientation on transformation-induced plasticity in multiphase carbon steels. *Model. Simul. Mater. Sci. Eng.* 14(4):617–36
193. Ramazani A, Mukherjee K, Quade H, Prahl U, Bleck W. 2013. Correlation between 2D and 3D flow curve modelling of DP steels using a microstructure-based RVE approach. *Mater. Sci. Eng. A* 560:129–39
194. Mahadevan S, Zhao Y. 2002. Advanced computer simulation of polycrystalline microstructure. *Comput. Methods Appl. Mech. Eng.* 191(34):3651–67
195. Kim JH, Lee M-G, Wagoner RH. 2010. A boundary smoothing algorithm for image-based modeling and its application to micromechanical analysis of multi-phase materials. *Comput. Mater. Sci.* 47(3):785–95

Contents

Modeling Active Mechanosensing in Cell–Matrix Interactions <i>Bin Chen, Baohua Ji, and Huajian Gao</i>	1
Biostructural Science Inspired by Next-Generation X-Ray Sources <i>Sol M. Gruner and Eaton E. Lattman</i>	33
Contemporary NMR Studies of Protein Electrostatics <i>Mathias A.S. Hass and Frans A.A. Mulder</i>	53
Anatomy of Nanoscale Propulsion <i>Vinita Yadav, Wentao Duan, Peter J. Butler, and Ayusman Sen</i>	77
Mechanisms of Autophagy <i>Nobuo N. Noda and Fuyuhiko Inagaki</i>	101
Single-Cell Physiology <i>Sattar Taberi-Araghi, Steven D. Brown, John T. Sauls, Dustin B. McIntosh, and Suckjoon Jun</i>	123
Roles for Synonymous Codon Usage in Protein Biogenesis <i>Julie L. Chaney and Patricia L. Clark</i>	143
Biophysics of Channelrhodopsin <i>Franziska Schneider, Christiane Grimm, and Peter Hegemann</i>	167
Structure and Mechanism of RNA Mimics of Green Fluorescent Protein <i>Mingxu You and Samie R. Jaffrey</i>	187
Regulation of Rad6/Rad18 Activity During DNA Damage Tolerance <i>Mark Hedglin and Stephen J. Benkovic</i>	207
Structure Principles of CRISPR-Cas Surveillance and Effector Complexes <i>Tsz Kin Martin Tsui and Hong Li</i>	229
Structural Biology of the Major Facilitator Superfamily Transporters <i>Nieng Yan</i>	257

Specification of Architecture and Function of Actin Structures by Actin Nucleation Factors <i>Colleen T. Skau and Clare M. Waterman</i>	285
Structural Symmetry in Membrane Proteins <i>Lucy R. Forrest</i>	311
The Synaptic Vesicle Release Machinery <i>Josep Rizo and Junjie Xu</i>	339

Index

Cumulative Index of Contributing Authors, Volumes 40–44	369
---------------------------------------------------------------	-----

Errata

An online log of corrections to *Annual Review of Biophysics* articles may be found at
<http://www.annualreviews.org/errata/biophys>